Design of a Thermally Balanced Membrane Reformer for Hydrogen Production

David S. A. Simakov and Moshe Sheintuch
Dept. of Chemical Engineering, Technion-Israel Institute of Technology, Haifa 32000, Israel

DOI 10.1002/aic.11568

Hydrogen production by autothermal methane steam reforming in a catalytic fixed bed membrane reactor has been analyzed and simulated. The two-compartment reactor indirectly couples the endothermic steam reforming with methane oxidation, while hydrogen is separated by a permselective Pd membrane. Simulations of the reactor, using published kinetics, map the acceptable domain of operation and the optimal set of operating parameters. The simulations exhibit slow-moving thermal fronts and the steady-state operation domains bounded by stationary fronts, separating domains of upstream and downstream-moving fronts. Front velocity depends on thermal coupling and hydrogen separation. An analytical approximation for the thermal front velocity in a thermally balanced reactor has been developed. © 2008 American Institute of Chemical Engineers *AIChE J,* 54: 2735–2750, 2008

Keywords: hydrogen, steam reforming, autothermal reforming, membrane reactor, thermal front

Introduction

Hydrogen is a very promising environmentally friendly fuel that can be used for efficient and clean electricity production using fuel cells but its purification and transportation are quite challenging. These drawbacks may be overcome when hydrogen is generated on-site using a catalytic membrane reactor, where hydrogen is produced over the catalyst bed (commonly by reforming or dehydrogenation of hydrocarbons) and simultaneously separated by a permselective membrane (e.g., Pd).

The use of a membrane shifts the reaction equilibrium toward hydrogen production, yielding high conversions at relatively lower temperatures, as well as it provides pure hydrogen. Since reforming is highly endothermic, the membrane reactor should be operated autothermally, with the heat required supplied by an exothermic oxidation by direct or indirect heat exchange. Such small-to-medium scale mobile devises for hydrogen production are likely to be more efficient than energy-demanding water electrolyzers and they may be a good solution for fuel cell cars, stationary fuel cell power stations, etc.

Hydrogen production in membrane reactors via methane steam reforming (MSR),[1–8] methanol steam reforming (MetSR),[9–14] methane dry reforming (MDR),[15–17] and hydrocarbons dehydrogenation (HDH)[18–21] has been extensively investigated in the last two decades. Steam reforming of methane is of remarkable interest, since there are large resources of natural gas in the world; steam can also be easily supplied. Even though carbon dioxide is still produced in the steam reforming process, its production per unit energy produced can be significantly reduced since the efficiency of fuel cells is considerably higher than that of combustion engines. Moreover, the concentration of carbon dioxide in the reactor effluent can be reduced, for example, by sorption in an additional fluidized bed unit.[22] When conversion is complete, the stream exiting the reformer contains only water and CO_2, which can be compressed and stored after condensation.

Metallic membranes (Pd or Pd alloys) are typically used for hydrogen separation,[1–11,16–19] either as an unsupported

---

Correspondence concerning this article should be addressed to D. S. A. Simakov at simakov@tx.technion.ac.il or M. Sheintuch at cermsll@technion.ac.il.

foil or as a thin film supported on a porous (ceramic or stainless steel) tube to improve the membrane strength. Pd membranes provide almost complete selectivity to hydrogen, but their cost is high. The potentially inexpensive molecular sieve zeolitic,[20,21] silica,[15,23–27] and carbon[14,28] membranes were considered as alternative candidates to the expensive Pd membranes. However, they offer low selectivity to hydrogen and there are still drawbacks in their preparation technology.

The most commonly used design of membrane reactors for hydrogen production is packed bed membrane reactor (PBMR)[1–5,9–11,13–17,18–21,23,29,27,28,30]; few studies employed a fluidized bed membrane reactor (FBMR).[6–8] The operation of a lab-scale PBMR for MetSR,[9,13,14] MDR,[15–17] and HDH,[18,20,21,26] and the use of FBMR for MSR[8] were experimentally investigated in numerous works. To establish a trans-membrane hydrogen partial pressure gradient, a lower pressure (or vacuum) is kept in the permeate side; frequently, hydrogen is also swept by N_2 or steam. The required heat in experimental studies is provided by an electrical furnace. Most theoretical works employ a homogeneous, steady-state, one-dimensional, plug flow, isobaric model, while isothermal conditions are commonly assumed.[1,3–5,10,11,18]

To provide the enthalpy required for the endothermic process, the reactor should be coupled to a heat source or to an exothermic reaction. Coupling of exothermic and endothermic reactions can be achieved by regenerative coupling (alternating feeds in a reverse-flow reactor), direct coupling (DC), where both reactions take place over the same catalyst bed, or by indirect coupling (IC) using counter-current or co-current heat exchange reactor. One of the major drawbacks in the DC and reverse flow reactors is catalyst selection, since the catalyst should favor both exothermic and endothermic reactions and withstand the hotspots emerging due to the exothermic reaction. Also, hydrogen is very reactive and will be produced in a DC unit only after oxygen has been consumed, whereas nitrogen (when the reactor is fed by air) will dilute the stream, suppressing the separation due to diminished pressure gradient. These constraints can be overcome in the IC reactors, where the endothermic and exothermic reactions are separated in space, also enabling operational flexibilities, since the operating parameters of exothermic and endothermic compartments can be independently adjusted. Co-current operation has been claimed to be preferable, as it allows for lowering the temperature peak, which is one of the drawbacks in the counter-current IC reactors[31]; yet, considerations of heat dispersion and reactor dynamics may change this result.

Coupling MetSR and HDH with oxidation in a lab-scale PBMR[32–37] has been experimentally investigated in several works. Experimental investigation of MetSR[38] and MSR[39] coupled with oxidation in a lab-scale packed bed reactor (PBR) without hydrogen separation membrane has also been reported. The endothermic and exothermic reactions were performed in the same reactor compartment, i.e., oxygen was co-fed to the reactor.[35–37,39] In a recent work,[38] axial distribution of air through porous ceramic membranes along the reactor was employed to limit the temperature peak within the catalyst bed. In other experimental works, the endothermic and exothermic reactions were coupled indirectly: oxygen was added to the permeate side to combust some fraction of hydrogen separated[32,33] or the reactor effluent was oxidized in an additional external packed bed tube.[34] Experimental investigations of monolith and microchannels reactors for coupling of MSR with methane oxidation (MOx) in adjacent channels (with heat transfer between them) have also been reported.[40,41]

The majority of the reported simulation works investigate DC of MSR with MOx in PBMR[31,42] and FBMR[43–45] with Pd-based membranes or in PBR.[46–48] Simulations of MSR with MOx coupled indirectly using a packed bed heat exchange reformer (without membrane),[49] a monolith reactor,[40,50] and a microchannel reactor[41] have also been reported. Steady-state conditions and negligible thermal dispersion (for packed beds) are typically assumed in the simulations; only few works investigate dynamic behavior[31,48–50] and account for thermal dispersion.[31,48]

Accounting for thermal dispersion is essential in such models as thermal (creeping) fronts may develop and move through the systems; such a term is missing in most studies. Moreover, obtaining the steady-state solution is insufficient and inefficient for analysis, even when heat dispersion is accounted for, since it may yield unstable solutions and since dynamics is an essential part of understanding reactor behavior; also, obtaining the steady solution of the boundary-value problem is not numerically faster than the transient analysis.

Thermal fronts, moving due to heat convection and heat dispersion, are expected to occur in fixed bed catalyzing oxidation reactions (e.g., MOx). This phenomenon is particularly important for IC co-current reactors, since their limiting throughput is determined by the conditions that induce downstream propagating fronts, which will eventually result in extinction. Simulations of such reactors combined with hydrogen membrane separation, i.e., IC of MSR with MOx in PBMR for hydrogen production, are lacking. In fact, as we show later, the limiting throughput of the IC PBMR reactor is determined by the front propagation features and its steady-state location.

This article is aimed at designing a thermally balanced PBMR that continuously produces ultrapure hydrogen, while the reformer (MSR) and oxidizer (MOx) are indirectly coupled and the oxidizer provides the enthalpy for both the endothermic reaction and for heating up the feed. We focus on examining slow-moving thermal fronts propagating in the reactor and show that the process operating domain is defined by their dynamics. The key parameters and operating domain boundaries were found using thermodynamic considerations, detailed parametric numerical study, and analytical solution.

Reactor Model and the Asymptotes

Kinetics

The following reactions describe the stoichiometry and the thermochemistry of MSR:

$$CH_4 + H_2O = CO + 3H_2 \quad \Delta H_{\mathrm{I}} = 206\,\mathrm{kJ/mol} \tag{1a}$$

$$CO + H_2O = CO_2 + H_2 \quad \Delta H_{\mathrm{II}} = -41\,\mathrm{kJ/mol} \tag{1b}$$

$$CH_4 + 2H_2O = CO_2 + 4H_2 \quad \Delta H_{\mathrm{III}} = 165\,\mathrm{kJ/mol} \tag{1c}$$

In the simulations, we use the commonly employed rate expressions developed by Xu and Froment[51] for MSR over a Ni/Al_2O_3 catalyst:

$$R_{\mathrm{I}} = \frac{k_{\mathrm{I}}}{p_{\mathrm{H_2}}^{2.5}}\left(p_{\mathrm{CH_4}}p_{\mathrm{H_2O}} - \frac{p_{\mathrm{H_2}}^{3}p_{\mathrm{CO}}}{K\mathrm{eq_I}}\right)\frac{1}{\mathrm{den}^2} \tag{2a}$$

$$R_{\mathrm{II}} = \frac{k_{\mathrm{II}}}{p_{\mathrm{H_2}}}\left(p_{\mathrm{CO}}p_{\mathrm{H_2O}} - \frac{p_{\mathrm{H_2}}p_{\mathrm{CO_2}}}{K\mathrm{eq_{II}}}\right)\frac{1}{\mathrm{den}^2} \tag{2b}$$

$$R_{\mathrm{III}} = \frac{k_{\mathrm{III}}}{p_{\mathrm{H_2}}^{3.5}}\left(p_{\mathrm{CH_4}}p_{\mathrm{H_2O}}^{2} - \frac{p_{\mathrm{H_2}}p_{\mathrm{CO_2}}}{K\mathrm{eq_{III}}}\right)\frac{1}{\mathrm{den}^2} \tag{2c}$$

$$\mathrm{den} = 1 + K_{\mathrm{CO}}p_{\mathrm{CO}} + K_{\mathrm{H_2}}p_{\mathrm{H_2}} + K_{\mathrm{CH_4}}p_{\mathrm{CH_4}} + \frac{K_{\mathrm{H_2O}}p_{\mathrm{H_2O}}}{p_{\mathrm{H_2}}}$$

$$k_j = A_j \exp\left(\frac{-E_j}{R_g T}\right), \quad j = \mathrm{I, II, III};$$

$$K_i = B_i \exp\left(\frac{-\Delta H_i}{R_g T}\right), \qquad i = \mathrm{CH_4, H_2O, CO, CO_2, H_2}$$

Complete oxidation of methane (MOx) is given by the following reaction:

$$\mathrm{CH_4 + 2O_2 = CO_2 + 2H_2O} \quad \Delta\mathrm{H_{Ox}} = -803\,\mathrm{kJ/mol} \tag{3}$$

Of the several kinetic models proposed to describe the intrinsic kinetics of MOx on various catalysts (Pt, Pd, Ni, etc.), we use the Langmuir-Hinshelwood rate equation[52,53] for MOx over a Ni/Al_2O_3 catalyst:

$$R_{\mathrm{IV}} = \frac{k_{1a}p_{\mathrm{CH_4}}p_{\mathrm{o_2}}}{(1 + K_{\mathrm{CH_4}}^{\mathrm{ox}}p_{\mathrm{CH_4}} + K_{\mathrm{O_2}}^{\mathrm{ox}}p\mathrm{o_2}})^2 + \frac{k_{1b}p_{\mathrm{CH_4}}p_{\mathrm{o_2}}}{(1 + K_{\mathrm{CH_4}}^{\mathrm{ox}}p_{\mathrm{CH_4}} + K_{\mathrm{O_2}}^{\mathrm{ox}}p_{\mathrm{O_2}})} \tag{4}$$

$$k_j = A_j \exp\left(\frac{-E_j}{R_{\mathrm{g}} T}\right), \quad j = 1a, 1b;$$

$$K_i^{\mathrm{ox}} = B_i \exp\left(\frac{-\Delta H_i}{R_{\mathrm{g}} T}\right), \quad i = \mathrm{CH_4, O_2}$$

Reactor model

A schematic representation of the simulated reactor is shown in Figure 1. The reactor is assumed to be composed of two concentric cylinders: a fixed bed for steam reforming reaction, which contains one or several Pd membranes, is surrounded by an outer tube packed with a catalyst for oxidation reaction. The transient one-dimensional enthalpy and mass balances presented later represent a standard pseudo-homogeneous model of a fixed bed reactor containing different compartments with heat and mass exchange between them. Axial thermal and mass dispersion are accounted, and the following assumptions are made:

(i) Overall adiabatic operation,

(ii) The membrane is permeable only to hydrogen (by Seivert's law),

(iii) Negligible radial mass and heat dispersion,

(iv) Negligible axial pressure drop,

(v) Ideal gas, and

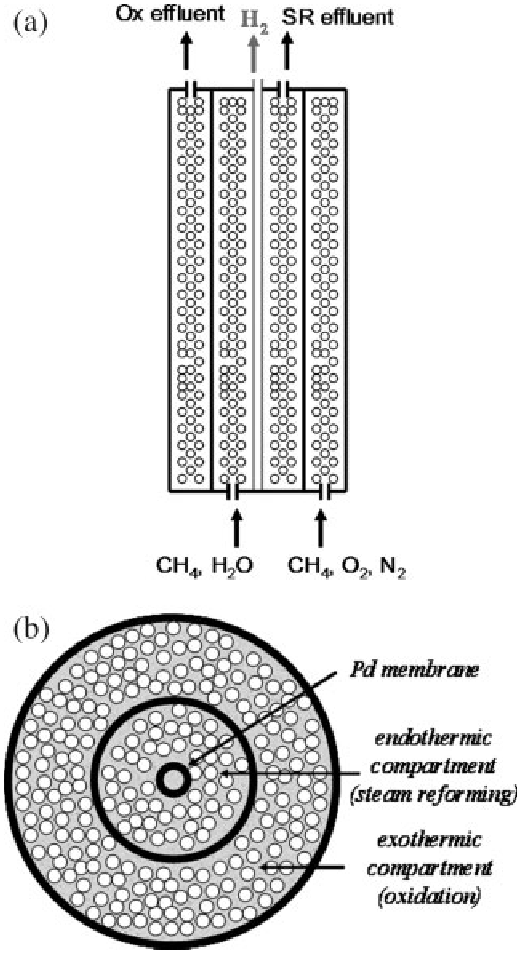

Figure 1. (a) Schematic of the simulated reactor with entering and exiting gas flows; (b) corresponding cross-sectional view of (a).

(vi) Constant thermophysical properties (pressure and temperature dependences are accounted for)

$$(\varepsilon\rho_{\mathrm{g}}C_{\mathrm{pg}} + (1-\varepsilon)\rho_{\mathrm{s}}C_{\mathrm{ps}})^k \frac{\partial T^k}{\partial t} = k_{ae}^k \frac{\partial^2 T^k}{\partial z^2} - (\varepsilon\rho_{\mathrm{g}}v_{\mathrm{g}}C_{\mathrm{pg}})^k \frac{\partial T}{\partial z} + \rho_s^k(1-\varepsilon^k)\sum_j(-\Delta H_j)R_j - a_{\mathrm{vh}}^k U_w \Delta T^k \tag{5}$$

$$(\varepsilon\rho_{\mathrm{g}})^k \frac{\partial y_i^k}{\partial t} = (\rho_{\mathrm{g}}D_{\mathrm{ae}})^k \frac{\partial^2 y_i^k}{\partial z^2} - (\varepsilon\rho_{\mathrm{g}}v_{\mathrm{g}})^k \frac{\partial y_i^k}{\partial z} + \rho_s^k(1-\varepsilon^k)\sum_j \alpha_{ij}R_j - a_{\mathrm{vm}}^k A_i \exp\left(\frac{-E_a}{R_g T^k}\right)\Delta\left(\sqrt{p_i}\right)^k \tag{6}$$

$$k \equiv \mathrm{SR, Ox, M}, \quad i = \mathrm{CH_4, H_2O, O_2, CO, CO_2, H_2}, \quad j \equiv \mathrm{I - IV}$$

$$a_{\mathrm{vh}}^k = \frac{S^{\mathrm{SR}}}{V^k}, \ a_{\mathrm{vm}}^k = \frac{S^{\mathrm{M}}}{V^k}, \quad v_{\mathrm{g}}^k = \frac{Q_{\mathrm{tf}}^{\mathrm{k}}}{\varepsilon A_{\mathrm{cs}}^k}, \quad p_i = y_i P_t, \quad A_i = 0$$

for $i \neq H_2$

$$\Delta T^{\mathrm{SR}} = T^{\mathrm{SR}} - T^{\mathrm{Ox}}; \quad \Delta T^{\mathrm{Ox}} = -\Delta T^{\mathrm{SR}},$$

$$\Delta\left(\sqrt{p_i}\right)^{\mathrm{SR}} = \sqrt{p_i^{\mathrm{SR}}} - \sqrt{p_i^{\mathrm{M}}}; \quad \Delta\left(\sqrt{p_i}\right)^{\mathrm{M}} = -\Delta\left(\sqrt{p_i}\right)^{\mathrm{SR}}$$

Note that changes in molar density have been neglected. Even though Eq. 1c predicts an increase in the number of moles as a result of the SR reaction, total molar density changes can be neglected, since a significant part of H_2 is separated by the membrane. The following characteristic for Pd membranes values (adopted from the literature) were used for hydrogen permeation parameters:

$$A_{\mathrm{H}_2} = 6.7\,\frac{\mathrm{mol}}{\mathrm{m}^2\,\mathrm{s}\,\mathrm{MPa}^{0.5}}, \quad E_\mathrm{a} = 15\,\frac{\mathrm{kJ}}{\mathrm{mol}}$$

Radial mass gradients of hydrogen were neglected, even though hydrogen is extracted through the membrane, since its mixing rate (ratio of dispersion to tube radius, $D_\mathrm{r}/r \approx 10^{-2}\mathrm{m/s}^{54}$) is an order of magnitude higher than the hydrogen permeation scale calculated from Seivert's law at the front conditions ($A_{\mathrm{H}_2}\Delta(p_{\mathrm{H}_2}^{0.5})\exp(-E_\mathrm{a}/R_\mathrm{g}T) \approx 10^{-3}\mathrm{m/s}$), this rate will be smaller downstream, as the hydrogen gradient declines. Radial heat gradients are usually ignored in adiabatic reactors; in our study, the whole system is adiabatic and we expect radial gradients to be negligible.

An infinite heat transfer coefficient between the membrane inner and the SR compartment is assumed ($T^\mathrm{M} = T^\mathrm{SR}$) and the axial dispersion term in the membrane interior is neglected, i.e., $(p_\mathrm{g}D_\mathrm{ae})^\mathrm{M} = 0$; also, $y_\mathrm{if}^\mathrm{M} = 0$. The following boundary (Danckwert's) and initial conditions are used:

$$z = 0\colon\ (\varepsilon\rho_\mathrm{g}v_\mathrm{g}C_\mathrm{pg})^k(T_f^k - T^k) = -k_\mathrm{ae}^k\frac{\partial T^k}{\partial z}; \qquad (\varepsilon\rho_\mathrm{g}v_\mathrm{g})^k(y_{if}^k - y_i^k) = -(\rho_\mathrm{g}D_\mathrm{ae})^k\frac{\partial y_i^k}{\partial z} \tag{7a}$$

$$z = L\colon\quad \frac{\partial T^k}{\partial z} = 0; \quad \frac{\partial y_i^k}{\partial z} = 0 \tag{7b}$$

$$t = 0\colon\qquad T^k(0,z) = T_\mathrm{int}^k; \quad y_i^k(0,z) = y_{i,\mathrm{int}}^k \tag{8}$$

Since setting the feed hydrogen molar fraction ($y_{\mathrm{H}_2\mathrm{f}}$) to zero will lead to unbounded initial rate in Eqs. 2a–c, we set this value at $y_{\mathrm{H}_2\mathrm{f}} = 10^{-5}$. It was verified that the numerical solution is not sensitive to this value of $y_{\mathrm{H}_2\mathrm{f}}$. The reactor initial temperature of $T_\mathrm{int} = 650\,\mathrm{K}$ that allows for ignition for the given Ox kinetics was used in the simulations.

Transport coefficients

The overall radial wall heat transfer coefficient between the SR and oxidation (Ox) compartments is determined by resistances in series, i.e., accounting for resistances through the beds and the wall:

$$U_\mathrm{w} = \frac{1}{1/(h_\mathrm{we}^\mathrm{SR}) + d^w/(k_s^w) + 1/(h_\mathrm{we}^\mathrm{Ox})} \tag{9}$$

The effective radial wall heat transfer coefficient (h_we) for each reactor compartment is estimated from

$$Nu_\mathrm{we} \equiv \frac{h_\mathrm{we}d_\mathrm{p}}{k_\mathrm{g}} = 2.12\frac{k_\mathrm{rs}}{k_\mathrm{g}} + \beta_\mathrm{f}\left(8\frac{d_\mathrm{p}}{\mathrm{d_t}} + 2.12\right) \tag{10}$$

The term β_f corresponds to the effects of *RePr*, parameters for the individual phases, and the interphase heat transfer; its expression can be found in the original papers.[55,56] The correlated U_w values used in the simulations were in the range of $\approx 0.6 - 0.8\mathrm{kJ/(m^2\,s\,K)}$. These values are corresponding to the particle Nusselt number of $\approx$15−25 for the particle Reynolds number range of $\approx$1−60 used in the simulations, which is in line with the reported literature.[55,56]

The effective axial thermal dispersion coefficient is correlated from

$$\frac{1}{Pe_\mathrm{ae}} \equiv \frac{k_\mathrm{ae}}{\rho_\mathrm{g}v_\mathrm{g}C_\mathrm{pg}d_\mathrm{p}} = \frac{1}{Pe_\mathrm{af}} + \frac{k_\mathrm{as}/k_\mathrm{g}}{RePr\left\{1 + \frac{1}{N_\mathrm{s}}\left(\frac{8Bi_\mathrm{s}}{\mathrm{Bi_s}+4}\right)\right\}^2} \tag{11}$$

The correlation accounts for contributions of conduction in the gas phase (Pe_af is a function of *Re*, *Pr* and ε) and the solid. The definitions of parameters can be found in the original papers.[55,56] The characteristic k_ae values used in the simulations were in the range of $\approx 1\times10^{-3} - 1.2\times10^{-3}\mathrm{kJ/(m^2\,s\,K)}$, corresponding to the particle Peclet number of $\approx$0.1 − 1 for the particle Reynolds number range of $\approx$1 − 60 used in the simulations. This is in line with the reported literature.[55,56]

The effective axial mass dispersion coefficient is obtained from the following correlations[54]:

$$D_\mathrm{ae} = \varepsilon\frac{D_\mathrm{m}}{\tau}, \quad \text{for} \quad Re < 1; \qquad D_\mathrm{ae} = \varepsilon\left(\frac{D_\mathrm{m}}{\tau} + 0.5d_\mathrm{p}v_\mathrm{g}\right), \quad \text{for Re} > 5 \tag{12}$$

The correlated values of D_ae were in the range of $\approx 2 \times 10^{-4} - 6 \times 10^{-4}$ m^2/s, corresponding to the particle mass Peclet number of $\approx$0.1−5 for the particle Reynolds number range of $\approx$1−60.

Operating parameters

To reduce the number of parameters, let us find the adiabatic temperature change in a whole reactor coupling (indirectly) SR and Ox under the following assumptions: (i) infinite heat transfer between the SR and Ox reactor compartments; (ii) complete methane conversions; (iii) no CO formation, i.e., the SR process is represented by Eq. 2c; (iv) ideal gases. Assumption (iii) will hold for a high pressure in a long reactor, conditions that induce almost complete separation of hydrogen, consequently equilibrium shifts to final product (CO_2). Then, the adiabatic temperature rise is given by the following equation:

$$\Delta T_\mathrm{adc} = \frac{\sum_k(-\Delta H^k)y_\mathrm{mf}^kF_\mathrm{tf}^k}{\sum_k C_\mathrm{pg}^kF_\mathrm{tf}^k} = \frac{\sum_k(-\Delta H^k)y_\mathrm{mf}^kSV^kA_\mathrm{cs}^k}{\sum_k C_\mathrm{pg}^kSV^kA_\mathrm{cs}^k}, \quad k = \mathrm{SR, Ox} \tag{13}$$

$$\mathrm{SV}^k = \frac{1}{\tau^k} = \frac{Q_\mathrm{gf}^\mathrm{k}(\mathrm{STP})}{(\varepsilon\cdot V)^\mathrm{k}} = \frac{v_\mathrm{gf}^\mathrm{k}(\mathrm{STP})}{\mathrm{L}}$$

SV^k is gas hour space velocity, F_tf^k is total inlet molar flow, and A_cs^k is the cross-sectional area of the reactor compartment *k*.

The oxidation-to-steam reforming feed ratio is defined as follows:

$$R^* = \frac{F_{\mathrm{tf}}^{\mathrm{Ox}}}{F_{\mathrm{tf}}^{\mathrm{SR}}} \equiv \frac{\mathrm{SV}^{\mathrm{Ox}} A_{\mathrm{cs}}^{\mathrm{Ox}}}{\mathrm{SV}^{\mathrm{SR}} A_{\mathrm{cs}}^{\mathrm{SR}}} \equiv \frac{V_{\mathrm{g}}^{\mathrm{Ox}} A_{\mathrm{cs}}^{\mathrm{Ox}}}{V_{\mathrm{g}}^{\mathrm{SR}} A_{\mathrm{cs}}^{\mathrm{SR}}} \qquad (14)$$

Combining Eqs. 13 and 14, we express R^* as a function of methane feed concentrations and expected adiabatic temperature change:

$$R^* = \frac{\Delta T_{\mathrm{adc}} C_{\mathrm{pg}}^{\mathrm{SR}} - [(-\Delta H) y_{\mathrm{mf}}]^{\mathrm{SR}}}{[(-\Delta H) y_{\mathrm{mf}}]^{\mathrm{Ox}} - \Delta T_{\mathrm{adc}} C_{\mathrm{pg}}^{\mathrm{Ox}}} \qquad (15)$$

To obtain high steam reforming conversions, a sufficiently high temperature should be achieved. Preliminary simulations have shown that low methane conversions are obtained for ≈850 K, whereas when a reactor temperature of ≈900 K is achieved, conversions of $f^{\mathrm{Ox}} \approx 1$ and $f^{\mathrm{SR}} \approx 0.95$ can be obtained. Elevating temperature above ≈900 K is unfavorable, since it may damage the membrane and cause the catalyst sintering. Based on these considerations, we design for the reactor temperature of 900 K as an optimal one. Taking $y_{\mathrm{mf}}^{\mathrm{SR}} = 0.333$ (SR stoichiometry), $y_{\mathrm{mf}}^{\mathrm{Ox}} = 0.040$ (explosion limit), $y_{\mathrm{O_2f}}^{\mathrm{Ox}} = 2y_{\mathrm{mf}}^{\mathrm{Ox}}$ (Ox stoichiometry), and feed temperature equal to that required to evaporate water for a given SR operating pressure ($P_{\mathrm{t}}^{\mathrm{SR}} = 0.5-1$ MPa, $T_{\mathrm{f}} \approx 425-450$ K), we obtain $R^* \approx 4.1-3.9$, for which we design for.

To describe the reactor geometry for given feed space velocities, the $A_{\mathrm{cs}}^{\mathrm{Ox}}/A_{\mathrm{cs}}^{\mathrm{SR}}$ ratio is given by Eq. 14, and assuming the length-to-diameter ratio of $L/d_{\mathrm{t}} = 4$, which is convenient for tubular packed bed, we find

$$A_{\mathrm{cs}}^{\mathrm{Ox}} = \frac{R^* SV^{\mathrm{SR}} \pi \mathrm{L}^2}{64(SV^{\mathrm{Ox}} + R^* SV^{\mathrm{SR}})}; \quad A_{\mathrm{cs}}^{\mathrm{SR}} = \frac{\pi \mathrm{L}^2}{64} - A_{\mathrm{cs}}^{\mathrm{Ox}} \qquad (16)$$

Void fraction of $\varepsilon = 0.5$ and catalyst particle diameter of $d_{\mathrm{p}} = d_{\mathrm{t}}/30$ are assumed, and a geometric condition of $d_{\mathrm{t}}^{k} \leq 10d_{\mathrm{p}}$ (at least 10 catalytic particle in a radial direction) is imposed. To characterize the separation ability, the membrane area-to-SR compartment volume ratio is defined as follows:

$$\alpha_{\mathrm{v}}^{\mathrm{M}} = \frac{S^{\mathrm{M}}}{A_{\mathrm{cs}}^{\mathrm{SR}} L} \qquad (17)$$

Consequently, the problem is defined by five operating parameters: $\mathrm{SV}^{\mathrm{SR}}$, $\mathrm{SV}^{\mathrm{Ox}}$, $P_{\mathrm{t}}^{\mathrm{SR}}$, $a_{\mathrm{v}}^{\mathrm{m}}$, and L; the corresponding cross-sections are obtained from Eq. 16.

Results and Discussion

Typical results

The simulations performed have shown that once an ignition occurred, a slow-moving thermal front appears in the reactor. Drawing the acceptable domain of operation requires the characterization of this front. Thermal fronts are known to occur in fixed bed catalyzing exothermic reactions and the fronts move due to heat generation, convection, and heat dispersion. In the simulated coupled reactor system, the front motion is somewhat different due to the coupling of the exothermic reaction with the endothermic one and with hydrogen separation.

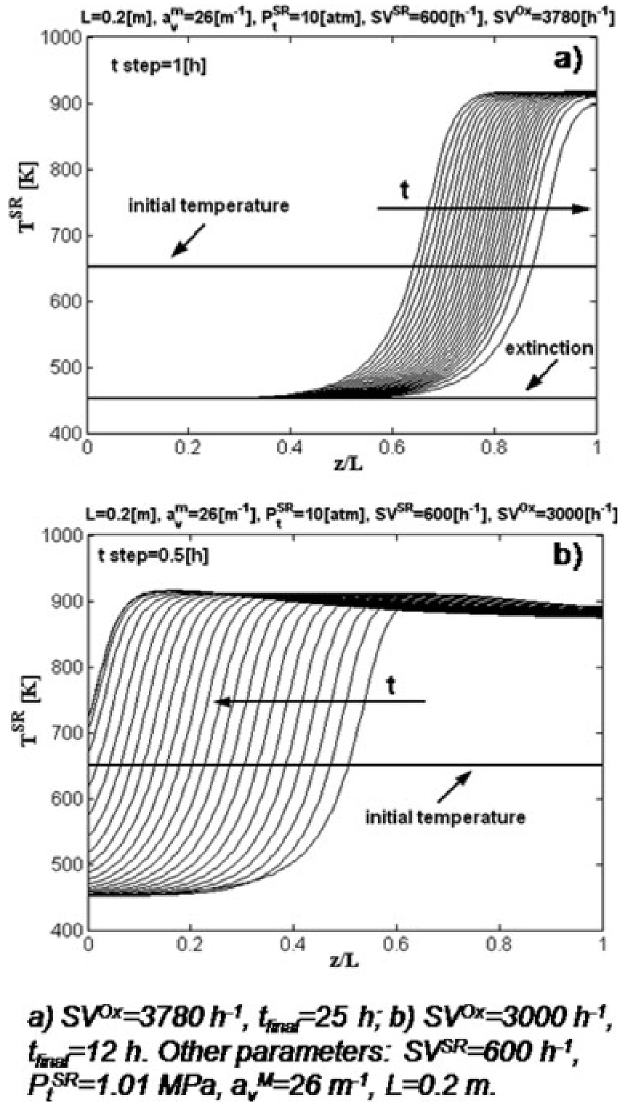

a) SV^{Ox}=3780 h^{-1}, t_{final}=25 h; b) SV^{Ox}=3000 h^{-1}, t_{final}=12 h. Other parameters: SV^{SR}=600 h^{-1}, P_t^{SR}=1.01 MPa, a_v^M=26 m^{-1}, L=0.2 m.

Figure 2. Typical downstream (a) and upstream (b) moving fronts.

Two typical examples of front propagation are presented in Figure 2, showing the spatial temperature profile of the steam reforming compartment for various times: the thermal front may propagate downstream (Figure 1a) or upstream (Figure 1b); increasing the space velocity in either the oxidation compartment ($\mathrm{SV}^{\mathrm{Ox}}$), or in the steam reforming compartment ($\mathrm{SV}^{\mathrm{SR}}$) will push the front downstream. Eventually, an extinguished or ignited steady state is achieved after the front has propagated downstream and exited or propagated upstream and stopped. The front propagation velocity is very small due to the high heat capacity of the solid phase (catalyst particles). The transient temperatures of the Ox and SR compartments were quite close to each other for all the simulations performed. This is due to the relatively high values of the wall heat transfer coefficient obtained from the correlations (section "Transport coefficients").

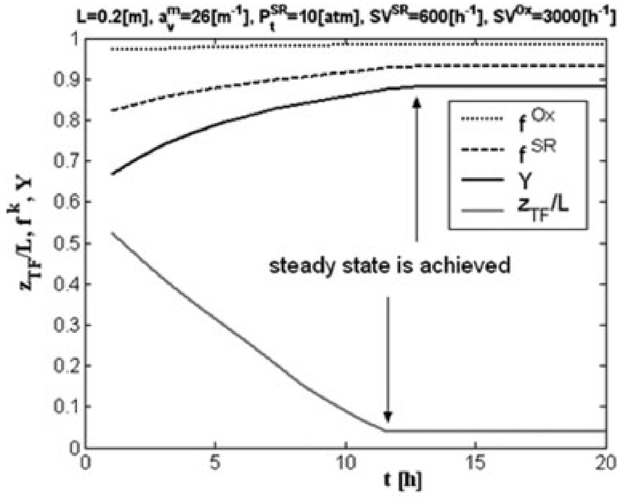

Parameters: SV^{SR}=600 h^{-1}, SV^{Ox}=3000 h^{-1}, P_t^{SR}=1.01 MPa, a_v^M=26 m^{-1}, L=0.2 m

Figure 3. Transient evolution of thermal front position, conversions, and hydrogen separation factor.

Temporal evolution of the dimensionless front position (z_{TF}/L) of methane conversions in the Ox and SR compartments (f^{Ox}, f^{SR}) and of hydrogen separation factor (Y) are shown in Figure 3 (for the case presented in Figure 1b); f^{Ox}, f^{SR} and Y gradually increase as the front propagates upstream and eventually reach their steady value, after the front has settled down. The thermal front position (z_{TF}) is defined by the location of its inflection point (i.e., $\partial^2 T/\partial z^2 = 0$). The hydrogen separation factor is defined as a ratio of moles of H_2 separated to moles of CH_4 fed to the SR compartment, normalized by the ideal value (Y_{max}), which is only limited by the transmembrane pressure gradient:

$$Y = \frac{F^{M}_{H_2,out}}{Y_{max} 4 F^{SR}_{mf}}, \quad Y_{max} = \left(1 - \frac{P^{M}_{t}}{P^{SR}_{t}}\right) \tag{18}$$

Transient thermal front position and respective propagation velocities are shown in Figures 4a, b. Increasing SV^{Ox} leads to increasing propagation velocities with a nearly linear relationship (Figure 4b). Front velocity ($v_{TF} = \partial z_{TF}/\partial t$) is calculated over a time interval after a fully developed front is formed until a steady state is established or until the front disappears. No ignition was obtained for $SV^{Ox} > 4300$ h^{-1} (with initially $T_{int} = 650$ K) and a stationary thermal front was immediately formed for $SV^{Ox} = 3650$ h^{-1}. Note, that while changing SV^{Ox} for a constant value of SV^{SR}, we also change the cross-sections of the SR and Ox compartments to keep R^* constant (Eqs. 14, 16).

Such linear dependence of v_{TF} on SV^{Ox} with a singular value of stationary thermal front (rather than a domain) has been observed for all the simulations performed and it is characteristic for thermal fronts in a fixed bed with a single simple-kinetics reaction. The simulations have also shown that the SR compartment space velocity (SV^{SR}) has a similar effect on v_{TF} (Figure 4c). The linear dependence of v_{TF} on

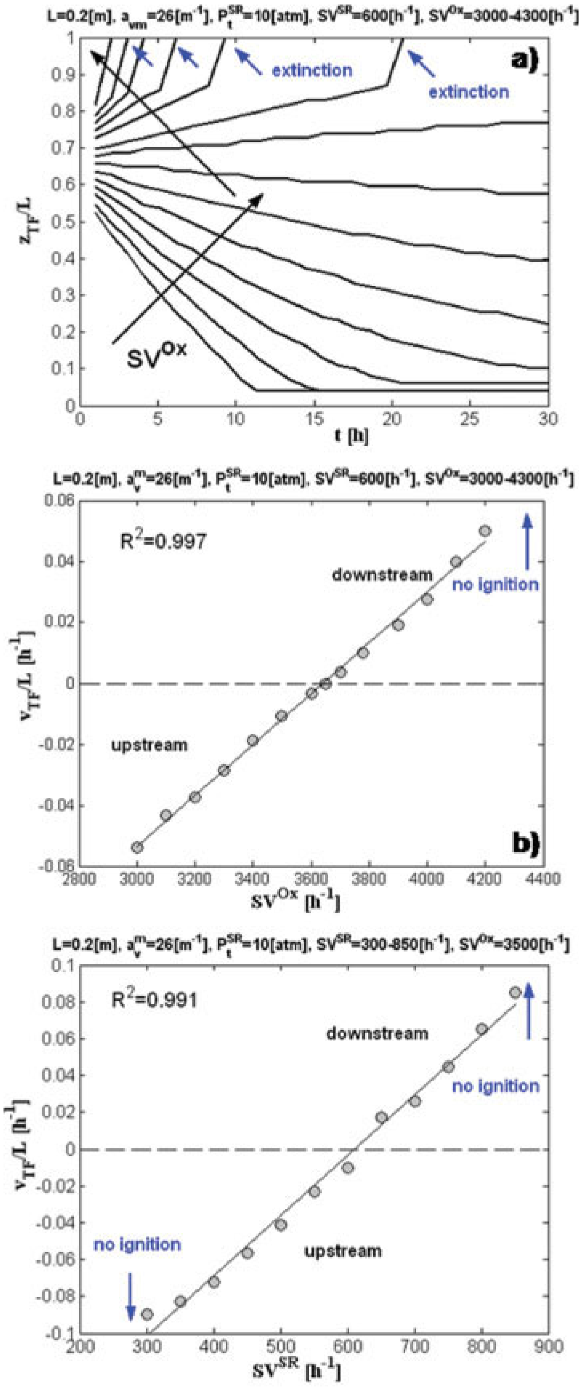

Parameters:
P_t^{SR}=1.01 MPa, a_v^M=26 m^{-1}, L=0.2 m.
(a) SV^{SR}=600 h^{-1}, SV^{Ox}=3000-4300 h^{-1};
(c) SV^{Ox}=3500 h^{-1}, SV^{SR}=300-850 h^{-1}.

Figure 4. (a) Transient thermal front position for various space velocities in the oxidation compartment; (b) thermal front velocities corresponded to Figure 4a; thermal front velocities for various space velocities in the steam reforming compartment.

[Color figure can be viewed in the online issue, which is available at www.interscience. wiley.com.]

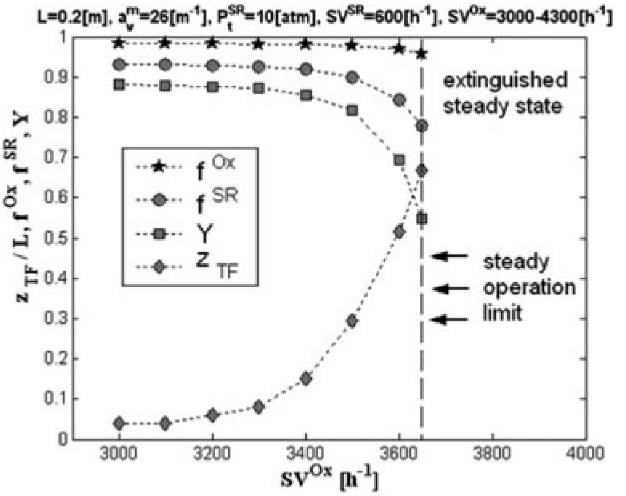

P_t^{SR}=1.01 MPa, a_v^M=26 m^{-1}, L=0.2 m.

Figure 5. Steady thermal front position, methane conversions, and hydrogen separation factor for various space velocities in the oxidation compartment.

the space velocity has been obtained for the fixed reactor geometry as well. These results are in line with the theoretical considerations discussed later (section "Thermal front velocity", Eq. 28).

Since one is interested in increasing throughput, while avoiding extinction, the stationary front solution is the limiting solution of the reactor, but not the optimal one. The optimal solution is a compromise between low z_{TF}, which will give good hydrogen yield and a high throughput. Increasing the space velocity causes thermal fronts to settle down at larger distances from the reactor inlet, reducing the part of the reactor involved in hydrogen separation. As a result, hydrogen separation efficiency decreases leading to lower f_{SR} and Y, Figure 5, where the steady sate values of z_{TF}, f^{Ox}, f^{SR}, and Y are plotted.

Typical steady-state profiles of temperature (T^{Ox}, T^{SR}), conversions (f^{Ox}, f^{SR}), efficiency (Y), and dimensionless molar flows of H_2 and CO (expressed as $F_i^* = F_i^{SR}/F_{tf}^{SR}$) are presented in Figures 6 and 7. In Figure 6, a limiting stationary thermal front case, showing a two zone (cold–hot) reactor, is presented. The front separates a cold zone upstream, with almost no reaction, from a reactive hot zone downstream. Since a constant pressure of 0.1 MPa was set up in the simulated membrane interior, some H_2 is observed in the cold zone (due to back H_2 transfer from the membrane interior to the SR compartment). H_2 is formed in the hot zone and simultaneously separated by the membrane. The length of the hot zone is not sufficient to maximally separate hydrogen, leading to relatively low values of f^{SR} and Y. For the front propagating upstream, a nearly isothermal reactor is obtained in steady state, Figure 7. In this case, most of the reactor is involved in the reaction/separation processes and the reactor can be operated more efficiently, yielding higher f^{SR} and Y. When a thermal front moves downstream, the front eventually exits the reactor and an extinguished case is obtained in steady state.

Figures 6 and 7 show that almost identical temperatures are obtained in both compartments for most of the reactor; the difference observed at the thermal front location is due to the heat transfer limitations. The values of the adiabatic temperature change obtained from the simulations (456 K and 425 K for Figures 6 and 7, respectively) were quite close to those calculated by Eq. 13 (450 K), and this similarity was also observed for other sets of parameters (for ignited cases); note that Eq. 13 assumes complete conversions of both SR and Ox processes and no CO formation.

CO outlet molar flow rates of $F_{CO}^{SR} \approx 0.08F_{tf}^{SR} - 0.1F_{tf}^{SR}$ were typically obtained, indicating that the CO extent is equilibrium-limited. This is dictated by the fact that the hydrogen separation efficiency is limited by the operating pressure in the membrane interior. This implies that the water gas shift (WGS) reaction (Eq. 1b) is not complete and the CO extent matches that expected by the WGS equilibrium at the operating temperature and intermembrane pres-

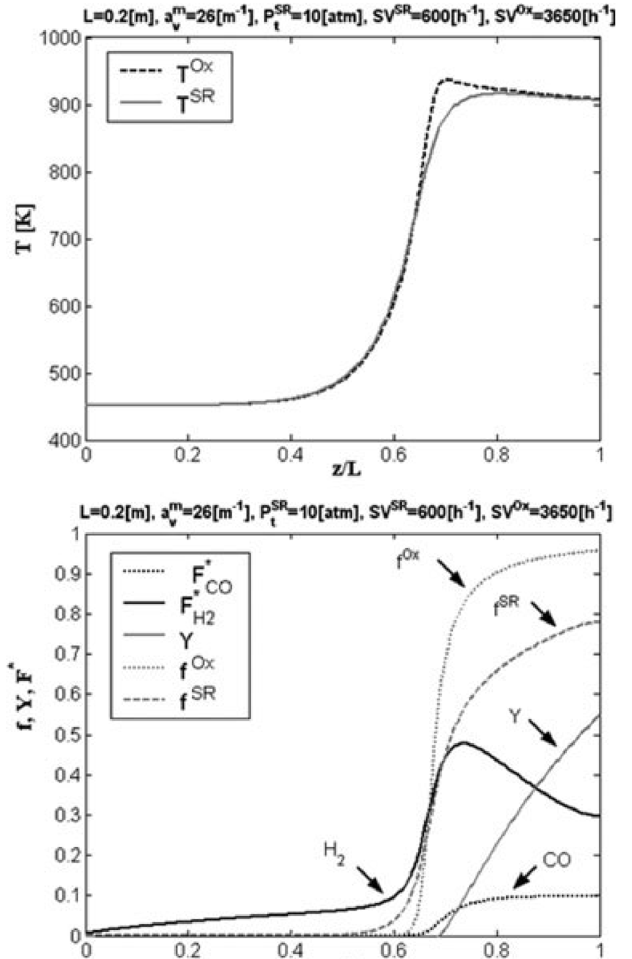

Parameters: SV^{SR}=600 h^{-1}, SV^{Ox}=3650 h^{-1},
P_t^{SR}=1.01 MPa, a_v^M=26 m^{-1}, L=0.2 m.

Figure 6. Steady profiles for the case of stationary thermal front.

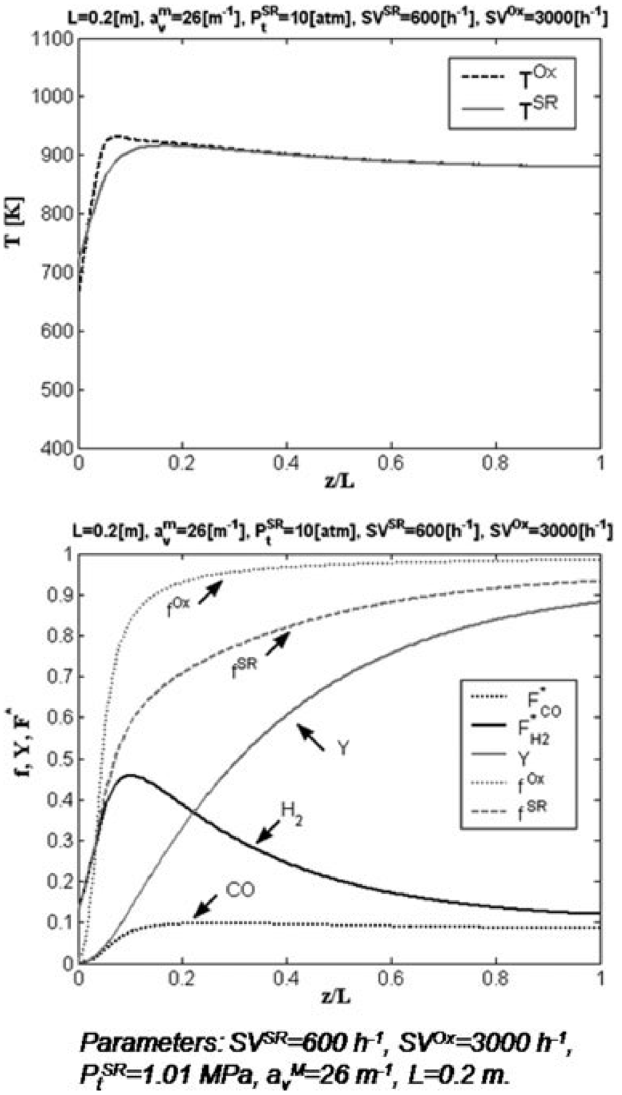

Figure 7. Steady profiles formed after the front propagated upstream resulting in a nearly isothermal reactor.

sure. Equilibrium analysis gives the following equation, which allows for calculating CO extent for given methane conversion (f_1) and transmembrane pressure difference (P_t^{SR}, P_t^M) (the derivation is given in Appendix):

$$\frac{(f_1 - f_2)(3 - 2f_1 + f_2)P_t^M}{f_2(2 - 2f_1 + f_2)(P_t^{SR} - P_t^M)} = 1.26 \times 10^{-2} \exp\left(\frac{4639}{T}\right), \quad F_{CO}^{SR} = F_{mf}^{SR} f_1 f_2 \qquad (19)$$

Equation 19 predicts well the results of the simulations; it estimates F_{CO}^{SR} of $\approx 0.07F_{tf}^{SR} - 0.09F_{tf}^{SR}$ for T = 900 K−950 K, f^{SR} = 0.95 (typical simulated values), P_t^M = 0.6−1 MPa, P_t^M = 0.1 MPa, and y_{mf}^{SR} = 0.33 (parameters used in the simulations). Since in the simulations the hydrogen separation does not reach equilibrium completely (implying $Y < 1$), the predicted equilibrium CO extent is slightly lower than the simulated values. To eliminate CO, the effluent may be further oxidized and the obtained energy can be used to preheat the reactor feed and to evaporate water for the SR compartment.

Operating window

Among the parameters that may influence the reactor performance, space velocities can be easily manipulated in a real H_2 generation unit. Figure 8 describes the acceptable steady-state domain of operation in the SV^{Ox} vs. SV^{SR} plane, while cross-sections obey Eqs. 14 and 16 to keep constant R^*; reactor length, operating pressure, and the membrane area-to-SR compartment volume ratio are kept constant. The operating domain is bounded by reactor geometry limits (dashed lines in Figure 8), which require each compartment to be larger than 10 catalyst particles in diameter. The other boundary marks the limiting conditions of upstream-moving fronts to induce an ignited reactor in steady state; beyond that boundary outside the domain marked by arrows fronts propagate downstream and eventually exit or no ignition occurs. Obviously, the initial reactor temperature must be sufficiently high to obtain the ignited state (the reactor initial temperature of T_{int} = 650 K that allows for ignition for the given Ox kinetics was used in the simulations).

The isolines in Figure 8 mark the steady-state dimensionless thermal front position (z_{TF}/L), steady-state methane SR conversion (f^{SR}) and hydrogen separation factor (Y). A nearly isothermal reactor, obtained for low space velocities, yields high f^{SR} and Y; increasing space velocities shifts z_{TF} toward the reactor exit, resulting in lower f^{SR} and Y, and eventually will lead to extinction. The extent of the SR reaction and the efficiency of the hydrogen separation are defined mainly by the location of the thermal front. The active high temperature part of the reactor has to be sufficiently long to efficiently separate hydrogen. If the active part of the reactor is too short to maximally separate hydrogen, relatively low values of f^{SR} and Y are obtained. Note that varying SV^{SR} and SV^{Ox} simultaneously, at a constant ratio, while satisfying Eq. 14 (implying fixed cross-sections), simulates the effect of increasing the system throughput, while maintaining the reactor geometry fixed.

Increasing the membrane area (α_v^M) reduces the size of operating window (Figure 9a). Enlarging the membrane area leads to more efficient hydrogen separation and, consequently, higher methane SR conversions. As a result, more heat is consumed leading to lower reactor temperatures, hence higher propagating downstream thermal front velocities (as it is described analytically in section "Thermal front velocity", Eq. 28). This should be compensated with lower space velocities, which in turn reduces the operating window.

In a real membrane reactor unit for hydrogen production, one is interested in maximizing hydrogen production. This requires operating at high space velocities in the SR reactor compartment, while keeping high Y. To achieve that, the reactor should be operated along the lower boundary of the operating window (geometry limit of $d_t^{SR} = 10d_p$). This gives the highest SV^{SR} for a given SV^{Ox}, while keeping sufficiently high Y (Figure 8). In Figure 9b, output hydrogen production rate ($Q_{H_2} l(STP)/min$) and Y are plotted vs. SV^{SR}

along the lower boundary of Figure 9a ($SV^{Ox} = 4.86\ SV^{SR}$, which implies constant cross-sections). Q_{H_2} passes through a maximum and declines with increasing SV^{SR}. Even though low membrane area allows to operate at higher SV^{SR}, less hydrogen is still obtained: lower Q_{H_2} and Y are obtained for $\alpha_v^M = 10\ m^{-1}$ than for $\alpha_v^M = 50\ m^{-1}$ over the whole range of SV^{SR}. One can conclude that the optimization between higher hydrogen output and higher membrane surface area should be based on economic considerations.

Similar optimization considerations are applied when the working pressure in the SR compartment (P_t^{SR}) are changed. For low (high) SV^{SR}, increasing P_t^{SR} leads to narrower (broader) operating window (Figure 10a). For low SV^{SR}, the P_t^{SR} effect is similar to that of the membrane area (Figure

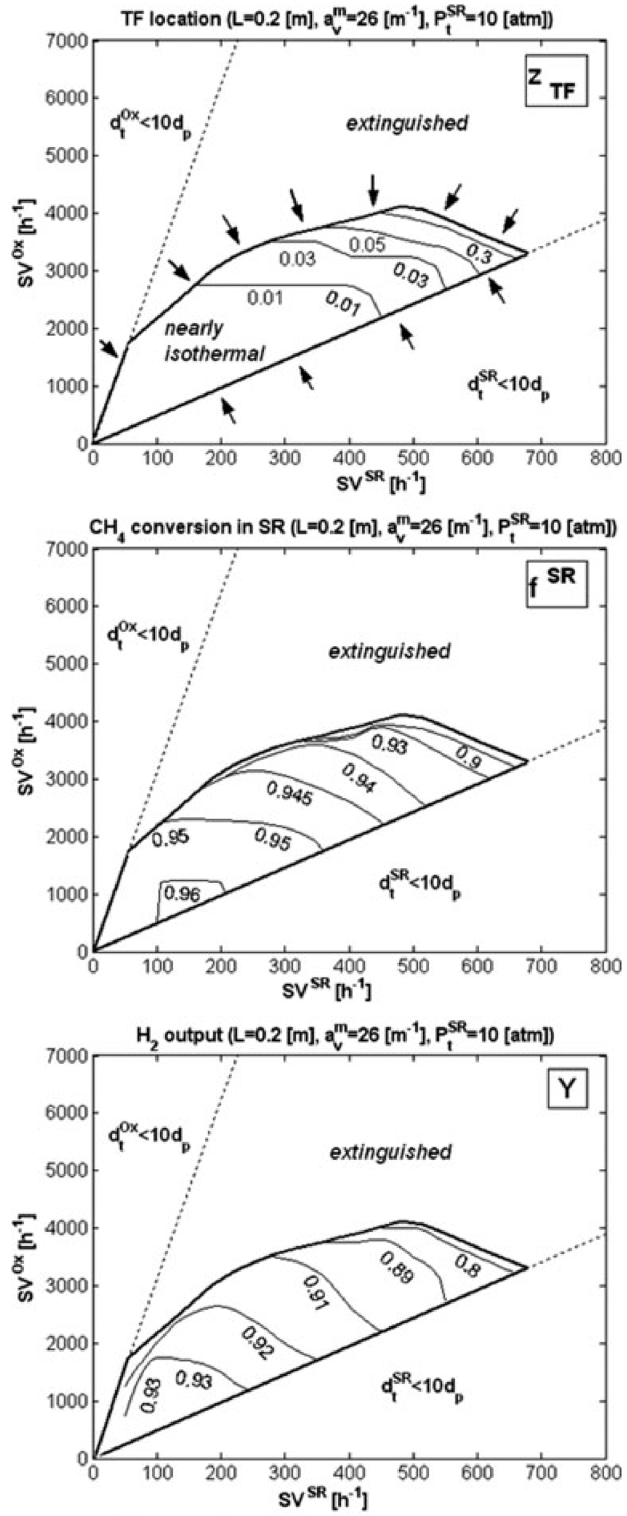

Parameters:
P_t^{SR}=1.01 MPa, a_v^M=26 m^{-1}, L=0.2 m.

Figure 8. Operating windows presented in the space velocities plane showing contours of thermal front position, methane steam reforming conversion, and hydrogen separation factor.

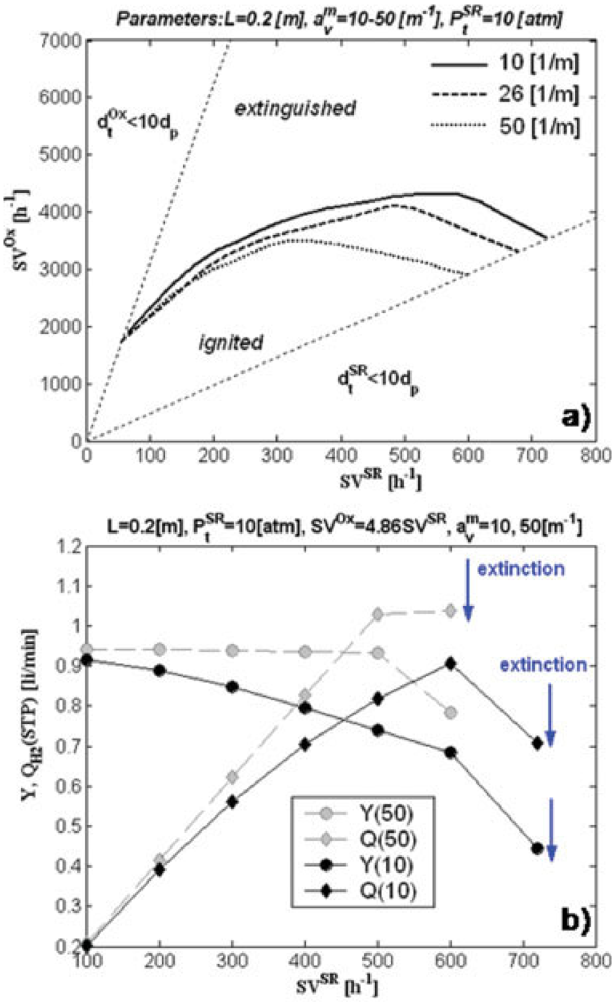

Parameters:
P_t^{SR}=1.01 MPa, a_v^M=10-50 m^{-1}, L=0.2 m.

Figure 9. (a) Effect of membrane area on the operating domain boundaries; (b) hydrogen separation factor and outlet volumetric flow rate along the lower boundary of (a); for avM = 10 m^{-1} (black line) and avM = 50 m^{-1} (gray line).

[Color figure can be viewed in the online issue, which is available at www.interscience.wiley.com.]

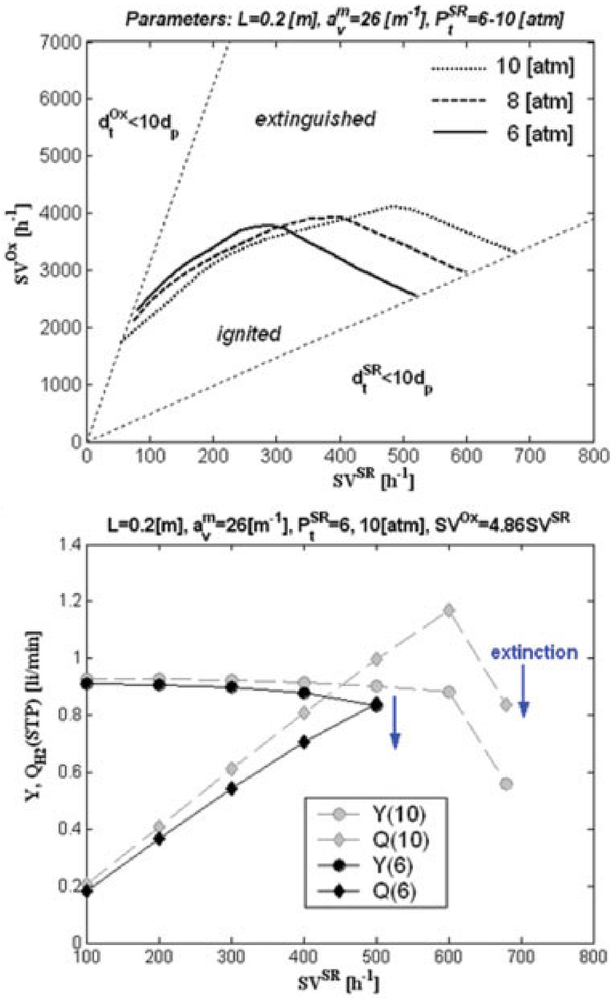

Parameters:
P_t^{SR}=0.61-1.01 MPa, a_v^M=26 m^{-1}, L=0.2 m.

Figure 10. Effect of the steam reforming operating pressure on (a) operating domain boundaries; (b) hydrogen separation factor and outlet volumetric flow rate along the lower boundary of (a); for PtSR = 0.608 MPa (black line) and PtSR = 1.01 MPa (gray line).

[Color figure can be viewed in the online issue, which is available at www.interscience. wiley.com.]

9a). Increasing P_t^{SR} improves hydrogen separation leading to higher f^{SR}, more heat consumption, lower reactor temperatures, and thermal fronts that tend to propagate downstream (section "Thermal front velocity", Eq. 28). This leads to extinction at lower space velocities, thus diminishing the operating window.

As SV^{SR} is increased, the effect of P_t^{SR} on the SR kinetics becomes dominant as it suppresses conversion and hydrogen generation. For high SV^{SR}, the kinetic effect of P_t^{SR} overcomes its separation effect, leading to higher reactor temperatures. Consequently, thermal fronts tend to propagate upstream (section "Thermal front velocity", Eq. 28), leading to extinction at higher space velocities, thus increasing the operating window. Plot of Q_{H_2} and Y vs. SV^{SR} (Figure 10b), along the lower restriction boundary (SV^{Ox} = 4.86 SV^{SR}) shows that the hydrogen output can be significantly improved by raising P_t^{SR}: Increasing P_t^{SR} leads to higher Q_{H_2} and Y for low SV^{SR} (due to the separation effect) and allows operating at higher SV^{SR} (due to the kinetic effect).

Extending the reactor length (L) increases the operating window (Figure 11a) up to a limit beyond which the operating window boundaries stay unchanged (L = 0.4 m for a given set of parameters). Note that the reactor diameter of d_t = 0.05 m is kept constant in Figure 11. Since the space velocity definition is $SV^k = v_g^k/L$, the results are presented in the gas velocity domain v^{Ox} vs. v^{SR} rather than in the SV^{Ox} vs. SV^{SR} plane. Increasing the reactor length above the limiting value does not influence the thermal front dynamics: Thermal fronts settle down at the same distance from the entrance and the same temperature profiles are obtained,

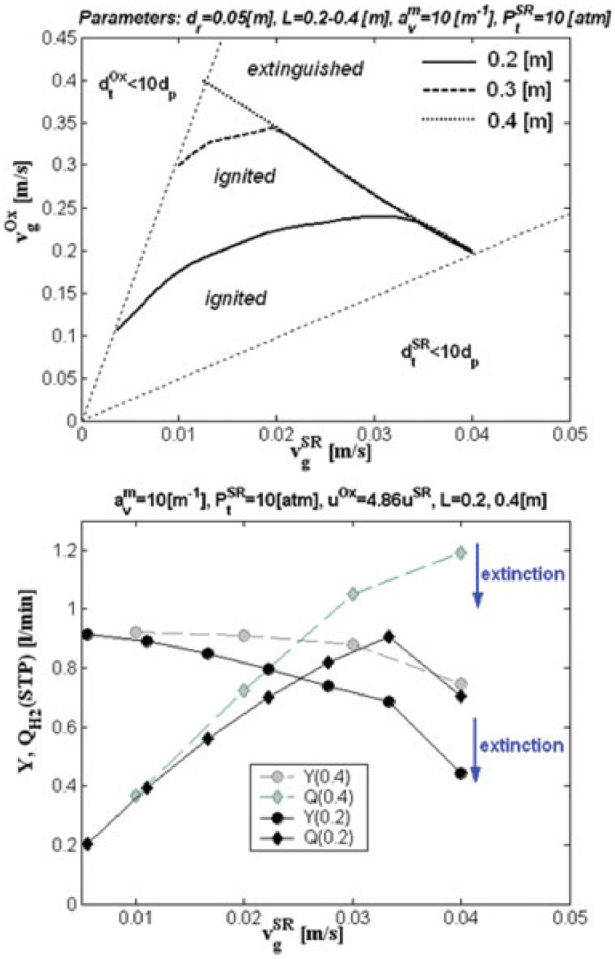

Parameters:
P_t^{SR}=1.01 MPa, a_v^M=10 m^{-1}, L=0.2-0.4 m.

Figure 11. Effect of reactor length on (a) operating window boundaries; (b) hydrogen separation factor and outlet volumetric flow rate along the lower boundary of (a); for *L* = 0.2 m (black line) and *L* = 0.4 m (gray line).

[Color figure can be viewed in the online issue, which is available at www.interscience.wiley.com.]

independently on L. On the other hand, the hydrogen output (Q_{H_2} and Y) is still slightly improved (Figure 11b, calculated along the lower operation window boundary). This effect is clearly attributed to the better hydrogen separation since more membrane is involved.

In designing a PBMR for hydrogen production, one is interested in maximizing the reactor throughput, while keeping the reactor conversions high. In terms of the operating window described earlier, it means that gas space velocities should be adjusted to keep the thermal front inside the reactor. In the following section, we show how the limiting gas velocities can be analytically estimated.

Once the limiting conditions were found, one should choose appropriate gas velocities inside the operating window, as well as the membrane area, operating pressure, and the reactor length (the cross-sections may be adjusted using Eq. 16). The trade-off between high throughput and high conversions will define the choice of the operating parameters. The highest conversions are attained when low gas velocities, which result in upstream-propagating fronts (ignited steady state) and high residence time (effective hydrogen separation, i.e., high Y), are used. The highest throughput is achieved along the lower boundary of the operating window.

As it was shown earlier, high-steam reforming operating pressures are preferable, while the membrane area should be selected considering the desired hydrogen output and the membrane cost. Also, the reactor length should be sufficient for initial ignition, reaction, and hydrogen separation. It should be kept in mind that changing parameters like membrane area, operating pressure, and reactor length may also significantly change the operating window boundaries (Figures 9–11).

Thermal front velocity

The operating domain was shown to be bounded by stationary fronts. Finding an expression for that boundary is the subject of this section. The approximate analytical expression is developed following an approach derived for a constant-pattern front moving in the fixed bed in which a single exothermic reaction is catalyzed.[57,58]

To obtain an analytical approximation, first we assume that the SR process can be described by the overall reaction, implying negligible formation of CO:

$$\mathrm{CH_4 + 2H_2O = CO_2 + 4H_2} \qquad \Delta H_{\mathrm{III}} = 165\,\mathrm{kJ/mol} \tag{1c}$$

Consequently, we account for two reactions (SR and Ox) that simultaneously occur in two indirectly coupled reactor compartments, as it is shown in Figure 1. It is also assumed that the SR rate is dictated by the rate of the Ox reaction and the SR reaction is fast enough to immediately reach equilibrium everywhere in the reactor. With the earlier assumptions, we have the following system of three differential equations (also neglecting axial mass dispersion):

$$\begin{aligned}(\rho C_\mathrm{p})^k_{\mathrm{eff}}\frac{\partial T^k}{\partial t} &= -\varepsilon(\rho C_\mathrm{p})_\mathrm{g} v_\mathrm{g}\frac{\partial T^k}{\partial z} + k^k_{\mathrm{ae}}\frac{\partial^2 T^k}{\partial z^2}\\ &\quad + \rho_\mathrm{s}(1-\varepsilon)(-\Delta H_k)R_k - a^k_{\mathrm{vh}}U_\mathrm{w}\Delta T^k, \quad k = \mathrm{Ox}, \mathrm{SR}\end{aligned} \tag{20}$$

$$\varepsilon\rho_\mathrm{g}^{\mathrm{Ox}}\frac{\partial y_\mathrm{m}^{\mathrm{Ox}}}{\partial t} = -\varepsilon(\rho v)_\mathrm{g}^{\mathrm{Ox}}\frac{\partial y_\mathrm{m}^{\mathrm{OX}}}{\partial z} - \rho_\mathrm{s}(1-\varepsilon)R_{\mathrm{Ox}} \tag{21}$$

We assume further that the heat transfer between the reactor compartments is fast enough, so that the temperature on both sides is identical. This assumption is supported by the simulations that showed identical temperature profiles in the SR and Ox compartments (except for a narrow region at the front maximal temperature, Figures 6 and 7). Now, the enthalpy balances given by Eq. 20 can be combined and the following equation with the averaged parameters is obtained:

$$\begin{aligned}\overline{Le}\frac{\partial T}{\partial t} &= -\overline{v_\mathrm{g}}\frac{\partial T}{\partial z} + \frac{\overline{(k_{\mathrm{ae}}/\rho_\mathrm{g})}}{\varepsilon C_{\mathrm{pg}}}\frac{\partial^2 T}{\partial z^2} + \frac{A^{\mathrm{Ox}}_{\mathrm{cs}}}{A^{\mathrm{SR}}_{\mathrm{cs}} + A^{\mathrm{Ox}}_{\mathrm{cs}}}\\ &\quad \times\left(1 - 0.21\frac{A^{\mathrm{SR}}_{\mathrm{cs}}\rho_\mathrm{g}^{\mathrm{Ox}}R_{\mathrm{SR}}}{A^{\mathrm{Ox}}_{\mathrm{cs}}\rho_\mathrm{g}^{\mathrm{SR}}R_{\mathrm{Ox}}}\right)\frac{(-\Delta H_{\mathrm{Ox}})}{\rho_\mathrm{g}^{\mathrm{Ox}}C_{\mathrm{ps}}}\rho_\mathrm{s}R_{\mathrm{Ox}}\end{aligned} \tag{22}$$

The average property (p) is defined as follows:

$$\bar{p} = p^{\mathrm{SR}}(1-\alpha) + p^{\mathrm{Ox}}\alpha \tag{23}$$

$$\alpha = \frac{A^{\mathrm{Ox}}_{\mathrm{cs}}}{A^{\mathrm{SR}}_{\mathrm{cs}} + A^{\mathrm{Ox}}_{\mathrm{cs}}}, \quad \bar{p} \equiv Le, v_\mathrm{g}, k_{\mathrm{ae}}/\rho_\mathrm{g},$$

$$Le = (\rho C_\mathrm{p})_{\mathrm{eff}}/(\varepsilon\rho C_\mathrm{p})_\mathrm{g}$$

Note that the terms $\pm S^{\mathrm{SR}}U_\mathrm{w}(T^{\mathrm{Ox}} - T^{\mathrm{SR}})$ in Eq. 20, accounting for inter-compartment heat transfer, cancel upon adding and $(-\Delta H_{\mathrm{SR}})/(-\Delta H_{\mathrm{Ox}}) = -0.21$. Also we set $\varepsilon = 0.5$, thus $(1-\varepsilon)/\varepsilon = 1$, and it is assumed that $C^{\mathrm{Ox}}_{\mathrm{pg}} = C^{\mathrm{SR}}_{\mathrm{pg}} \equiv C_{\mathrm{pg}}$. Since the SR and Ox compartments are operated at different pressures, the difference in molar gas densities is accounted for (via $k_{\mathrm{ae}}/\rho_\mathrm{g}$).

Finally, for a first-order oxidation reaction, the following two differential equations are obtained with corresponding initial and boundary (Danckwert's) conditions:

$$\overline{Le}\frac{\partial T}{\partial t} = -\overline{v_\mathrm{g}}\frac{\partial T}{\partial z} + \frac{\overline{(k_{\mathrm{ae}}/\rho_\mathrm{g})}}{\varepsilon C_{\mathrm{pg}}}\frac{\partial^2 T}{\partial z^2} + \frac{\alpha(-\overline{\Delta H})}{C_{\mathrm{pg}}}k^*_{\mathrm{Ox}}y_\mathrm{m}^{\mathrm{Ox}} \tag{24}$$

$$\frac{\partial y_\mathrm{m}^{\mathrm{Ox}}}{\partial t} = -\beta\overline{v_\mathrm{g}}\frac{\partial y_\mathrm{m}^{\mathrm{Ox}}}{\partial z} - k^*_{\mathrm{Ox}}y_\mathrm{m}^{\mathrm{Ox}} \tag{25}$$

$$z = -L/2: \quad \overline{v_\mathrm{g}}(T_f - T) = -\frac{\overline{(k_{\mathrm{ae}}/\rho_\mathrm{g})}}{\varepsilon C_{\mathrm{pg}}}\frac{\partial T}{\partial z}; \quad y_\mathrm{m}^{\mathrm{Ox}} = y_{\mathrm{mf}}^{\mathrm{Ox}} \tag{26a}$$

$$z = L/2: \qquad \frac{\partial T}{\partial z} = 0 \tag{26b}$$

$$t = 0: \qquad T(0,z) = T_{\mathrm{int}}, \quad y_\mathrm{m}^{\mathrm{Ox}}(0,z) = 0 \tag{27}$$

$$k^*_{\mathrm{Ox}} = A^*_{\mathrm{Ox}}\exp\left(-\frac{E_{\mathrm{Ox}}}{R_\mathrm{g}T}\right), \quad \beta = \frac{R^*}{\alpha(1+R^*)}$$

$$(-\overline{\Delta H}) = (-\Delta H_{\mathrm{Ox}})\left(1 - \frac{0.21\delta(1-\alpha)}{\alpha}\right), \quad \delta = \frac{\rho_\mathrm{g}^{\mathrm{Ox}}R_{\mathrm{SR}}}{\rho_\mathrm{g}^{\mathrm{SR}}R_{\mathrm{Ox}}}$$

$v_\mathrm{g}^{\mathrm{Ox}}$ in the mass balance is expressed in terms of $\overline{v_\mathrm{g}}$ using Eqs. 14 and 23. The single compartment Ox model is recovered when $A_{cs}^{SR} \rightarrow 0$ ($\alpha \rightarrow 1$, $(-\overline{\Delta H}) \rightarrow (-\Delta H_{Ox})$, $R^* \rightarrow \infty$, $\beta \rightarrow 1$, and $\overline{p} \rightarrow p^{Ox}$). We also assume that the ratio of the SR and Ox rates is constant everywhere in the reactor, implying $\delta = \text{const}$. The constant R_{SR}/R_{Ox} ratio should hold an average as R_{SR} is dictated by the rate of Ox due to the fast heat transfer between the reactor compartments.

Derivation of the front velocity approximation by solving Eqs. 24 and 25 is outlined in the Appendix. It yields two equations with respect to two unknown variables ω (dimensionless front velocity) and θ_{max} (dimensionless maximal temperature). Combining Eqs. A11 and A18 and rewriting it in dimensional form yields an equation that expresses the thermal front velocity (v^{TF}) as a function of the average gas velocity and maximal temperature (T_m):

$$v_{TF} = \frac{1}{Le}(\overline{v_g} - v_{TF0}),$$

$$v_{TF0} = \frac{T_m\sqrt{\alpha\overline{\Delta T}}}{(T_m - T_f)\sqrt{T_f}}\sqrt{\frac{A_{Ox}^*(\overline{k_{ae}/\rho_g})}{\varepsilon C_{pg}\gamma}\exp\left(-\frac{\gamma T_f}{T_m}\right)} \tag{28}$$

$$\overline{\Delta T} = \frac{(-\overline{\Delta H})y_{mf}^{Ox}}{C_{pg}}, \quad \gamma = \frac{E_{Ox}}{R_g T_f}$$

It was assumed that complete methane conversion is achieved in the Ox compartment, i.e., $x_m = 1$ and that the gas velocity is constant along the reactor, i.e., $\overline{v_g} = \overline{v_{gf}}$ and $\upsilon = 1$.

Equation 28 predicts a linear dependence of v^{TF} on $\overline{v_g}$ for constant T_m, which is in line with the simulations results (see section "Typical results"); the reactor temperature was kept nearly constant due to the thermodynamic constrain established in Eq. 15. Increasing T_m should lead to lower v^{TF} (Eq. 28), i.e., thermal fronts will tend to propagate upstream, in agreement with the simulation results (section "Operating window"). The influence of the endothermic reaction and the reactor geometry are accounted for via $-\overline{\Delta H}$ and α.

To estimate the operating domain boundary, we combine Eqs. A11 and A18, while $\omega = 0$, i.e., a stationary thermal front is obtained. Thus, the steady-state operation domain boundary (ODB) is approximated by

$$(\overline{v}_g)^{ODB} = \frac{\overline{T_m}\sqrt{\alpha}}{\lambda\sqrt{T_f\overline{\Delta T}}}\sqrt{\frac{A_{Ox}^*(\overline{k_{ae}/\rho_g})}{\varepsilon C_{pg}\gamma}\exp\left(-\frac{\gamma T_f}{\overline{T_m}}\right)} \tag{29}$$

$$\overline{T_m} = T_f + \lambda\overline{\Delta T}, \quad \lambda = \frac{R^*}{(1+R^*)}$$

$(\overline{v}_g)^{ODB}$ denotes the averaged feed velocity that will result in a stationary thermal front. For high R^*, $\lambda \rightarrow 1$, and $\overline{T}_m \rightarrow T_f + \overline{\Delta T}$, therefore increasing the oxidation-to-reforming feed ratio above $R^* \approx 5$ will not affect significantly $(\overline{v}_g)^{ODB}$. On the other hand, better (higher A_{Ox}^*) and less activated (lower γ) catalyst will increase $(\overline{v}_g)^{ODB}$.

In our case, the term $0.21\delta(1-\alpha)/\alpha$ in $-\overline{\Delta H}$ may be neglected, i.e., $(-\overline{\Delta H}) \rightarrow (-\Delta H_{Ox})$, since it is much lower than 1. This follows from the analysis of the characteristic values: α varies between 1 and 10, but R_{SR} is much lower than R_{Ox} and $\rho_g^{Ox}/\rho_g^{SR} \approx 0.1$ (SR compartment is operated at relatively high pressures). Negligible $0.21\delta(1-\alpha)/\alpha$ implies that the thermal front dynamics is independent on the SR kinetics. In terms of the original operating conditions (v_g^{Ox} vs. v_g^{SR}), the ODB line is expressed using Eqs. 14 and 23 as follows:

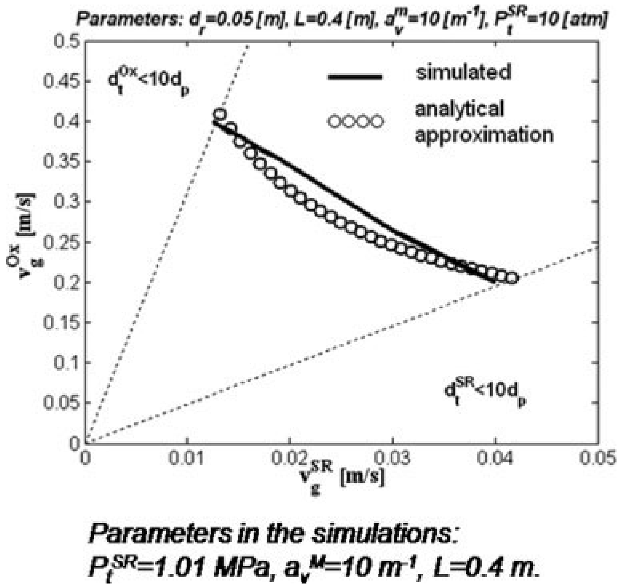

Figure 12. Operation domain boundaries obtained by the simulations (solid line) and calculated by Eqs. 30–31 (circles).

$$(v_g^{Ox})^{ODB} = \beta(\overline{v}_g)^{ODB} \equiv (\overline{v}_g)^{ODB}\frac{R^*}{\alpha(1+R^*)} \tag{30}$$

$$(v_g^{SR})^{ODB} = (\overline{v}_g)^{ODB}\frac{1}{(1-\alpha)(1+R^*)} \tag{31}$$

Note that once R^* is fixed then α is the only parameter that affects $(\overline{v}_g)^{ODB}$ and the two boundaries can be computed using α as a parameter. Figure 12 compares the results of the simulations with the developed analytical approximation (Eqs. 29–31), using the same parameters. The pre-exponent factor for a first-order kinetics (A_{Ox}^* s^{-1}) is the value used in the simulations (A_{Ox}mol/(MPa^2 s kg)), expressing it in appropriate units, i.e., $A_{Ox}^* s^{-1} = A_{Ox} \cdot (\rho_s/\rho_g) \cdot \langle y_{O_2f}^{Ox}\rangle$, $\langle y_{O_2f}^{Ox}\rangle = y_{O_2f}^{Ox}/2$. It can be seen that the analytical approximation estimates well the boundaries of the operation domain. Once the ODB has been determined, the reactor length and the membrane area, which will yield high conversion and efficient hydrogen separation, should be selected.

Conclusions

Hydrogen production in an autothermal membrane reformer coupling methane steam reforming with methane oxidation by indirect heat transfer and with hydrogen membrane separation has been analyzed numerically and analytically. Using thermodynamic and design considerations the problem was characterized by five key parameters: gas space velocities (in the steam reforming and oxidation compartments), the operating pressure in the SR compartment, the membrane area, and the reactor length. The influence of the key parameters on the operating domain boundaries has been studied by the simulations, aiming at finding the optimal sets of operating parameters.

Slow-moving thermal fronts were found to occur in the simulated reactor and the acceptable domain of steady-state operation was bounded by stationary fronts, separating domains of upstream and downstream-moving fronts. This domain has been mapped by the simulations. The operating domain boundary was approximated well by an analytical expression derived for that purpose.

We describe now the impact of the key parameters: Increasing throughput in the steam reforming compartment is accompanied by increasing flow rate in the oxidation compartment, to keep the reactor temperature around 900 K in order to achieve high conversions of the steam reforming reaction. Low-steam reforming conversions are obtained at lower temperatures, whereas higher temperatures may damage the membrane and cause catalyst deactivation. Gas space velocities should be kept below the operating domain boundary to keep the thermal front inside the reactor. The steam reforming operating pressures should be high enough to expedite hydrogen separation. Also, the membrane area and the reactor length should be sufficient for separation and reaction.

We suggest the following preliminary design procedure: (i) R^* (Eq. 15) should be chosen initially to achieve the desired maximal temperature; (ii) α (Eq. 23) is then chosen to obtain the operating boundary (Eqs. 30, 31); it also determines the ratio of cross-sections; (iii) the reactor length (catalyst weight) is determined now by the desired throughput; (iv) finally, the SR operating pressure and the membrane area are determined to provide sufficient hydrogen transfer area.

In future work, beside testing the indirect coupling concept experimentally, we will consider more efficient integration of the streams, like diverting the steam reforming effluent into the oxidation compartment to burn the residuals CO and H_2 and to use the resulting enthalpy. We will also examine the direct coupling approach.

Acknowledgments

This research was supported by US-Israel Binational Science Foundation and by Ministry of Science (Infrastructure Fellowship Program).

Notation

a_v = surface-to-volume ratio, m^{-1}
A_j = pre-exponential of the rate coefficient of a reaction, j[51–53]
A_{cs} = reactor compartment cross-sectional area, m^2
A_{H_2} = Pd membrane permeability, mol/(m^2 s MPa$^{0.5}$)
B_i = pre-exponential of the adsorption coefficient of a specie i[51–53]
Bi_s = solid-phase effective Biot number,[55,56]
C_{pg} = gas heat capacity, kJ/(mol K)
C_{ps} = gas heat capacity, kJ/(kg K)
d^w = reactor wall thickness, m
d_p = catalyst particle diameter, m
d_t = tube diameter, m
Da = Damköhler number
D_{ae} = effective axial mass dispersion, m^2/s[54]
D_m = gas molecular diffusivity, m^2/s
D_{re} = effective radial mass dispersion, m^2/s
E_a = Pd membrane activation energy, kJ/mol
E_j = activation energy for a reaction, j kJ/mol[51–53]
f = conversion
F = molar flow rate, mol/s
h_{we} = effective wall heat transfer coefficient kJ/(m s K)[55,56]
H = enthalpy, kJ/mol[51–53]
k_j = the rate coefficient of a reaction, j
K_i = the adsorption coefficient of a specie, i
k_{ae} = effective axial thermal conductivity, kJ/(m s K)
k_{as} = solid-phase effective axial thermal conductivity, kJ/(m s K)[55,56]
k_g = gas thermal conductivity, kJ/(m s K)
k_{re} = effective radial thermal conductivity, kJ/(m s K)[55,56]
k_{rs} = solid-phase effective radial thermal conductivity, kJ/(m s K)[55,56]
k_s^w = wall thermal conductivity, kJ/(m s K)
L = reactor length, m
Le = Lewis number
Nu_{we} = wall Nusselt number
p_i = partial pressure of a specie, i MPa
P_t = total pressure, MPa
Pe_{af} = fluid-phase axial Peclet number[55,56]
Pr = Prandtl number($C_{pg}\mu_g/k_g$)
Q = volumetric flow rate, l(STP)/min
r = radius, m
R_j = the rate of a reaction, j mol/(s kg)[51–53]
R_g = ideal gas constant, 8.314×10^{-3} kJ/(mol K)
Re = Reynolds number, ($\rho_g v_g d_p/\mu_g$)
S = reactor compartment surface, m
SV = gas space velocity, h^{-1}
t = time, s
T = temperature, K
U_w = overall effective wall heat transfer coefficient, kJ/(m s K)[55,56]
v_g = gas velocity, m/s
v_{TF} = thermal front velocity, m/s
V = reactor compartment volume, m^3
y_i = molar fraction of a specie, i
Y = hydrogen separation factor
z = reactor length coordinate, m
z_{TF} = thermal front position, m

Subscripts

f = feed
g = gas
int = initial
m = methane
s = solid
t = total

Abbreviations

Ox = oxidation compartment
SR = steam reforming compartment
M = membrane compartment

Greek letters

α_{ij} = the stoichiometric coefficient of a specie i in a reaction j
ε = void fraction
ϕ_i = the extent of a specie i
μ_g = gas viscosity, N s m^2
ρ_g = gas density, mol/m^3
ρ_s = solid density, kg/m^3
τ = tortousity

Literature Cited

1. Barbieri G, Di Maio FP. Simulation of the methane steam re-forming process in a catalytic Pd-membrane reactor. *Ind Eng Chem Res.* 1997;36:2121–2127.
2. Oklany JS, Hou K, Hughes R. A simulative comparison of dense and microporous membrane reactors for the steam reforming of methane. *Appl Catal A Gen.* 1998;170:13–22.

3. Hou K, Fowles M, Hughes R. Potential catalyst deactivation due to hydrogen removal in a membrane reactor used for methane steam reforming. *Chem Eng Sci*. 1999;54:3783–3791.
4. Kim JH, Choi BS, Yi J. Modified simulation of methane steam reforming in Pd-membrane packed-bed type reactor. *J Chem Eng Jpn*. 1999;32:760–769.
5. Gallucci F, Paturzo L, Basile A. A simulation study of the steam reforming of methane in a dense tubular membrane reactor. *Int J Hydrogen Energy*. 2004;29:611–617.
6. Adris AM, Lim CJ, Grace JR. The fluidized-bed membrane reactor for steam methane reforming: model verification and parametric study. *Chem Eng Sci*. 1997;52:1609–1622.
7. Abashar MEE. Coupling of steam and dry reforming of methane in catalytic fluidized bed membrane reactors. *Int J Hydrogen Energy*. 2004;29:799–808.
8. Patil CS, van Sint Annaland M, Kuipers JAM. Experimental study of a membrane assisted fluidized bed reactor for H_2 production by steam reforming of CH_4. *Chem Eng Res Des*. 2006;84:399–404.
9. Wielanda IS, Melina IT, Lamm IA. Membrane reactors for hydrogen production. *Chem Eng Sci*. 2002;57:1571–1576.
10. Harold MP, Naira B, Kolios G. Hydrogen generation in a Pd membrane fuel processor: assessment of methanol-based reaction systems. *Chem Eng Sci*. 2003;58:2551–2571.
11. Gallucci F, Paturzo L, Basile A. Hydrogen recovery from methanol steam reforming in a dense membrane reactor: simulation study. *Ind Eng Chem Res*. 2004;43:2420–2432.
12. Lattner JR, Harold MP. Comparison of methanol-based fuel processors for PEM fuel cell systems. *Appl Catal B Environ*. 2005;56:149–169.
13. Basile A, Tosti S, Capannelli G, Vitulli G, Iulianelli A, Gallucci F, Drioli E. Co-current and counter-current modes for methanol steam reforming membrane reactor: experimental study. *Catal Today*. 2006;118:237–245.
14. Zhang X, Hu H, Zhu Y, Zhu S. Methanol steam reforming to hydrogen in a carbon membrane reactor system. *Ind Eng Chem Res*. 2006;45:7997–8001.
15. Prabhu AK, Liu A, Lovell LG, Oyama ST. Modeling of the methane reforming reaction in hydrogen selective membrane reactors. *J Membr Sci*. 2000;177:83–95.
16. Múnera J, Irusta S, Cornaglia L, Lombardo E. CO_2 reforming of methane as a source of hydrogen using a membrane reactor. *Appl Catal A Gen*. 2003;245:383–395.
17. Ferreira-Aparicio P, Benito MJ. High performance membrane reactor system for hydrogen production from methane. *Ind Eng Chem Res*. 2005;44:742–748.
18. Sheintuch M, Dessau RMD. Observations, modeling and optimization of yield, selectivity and activity during dehydrogenation of isobutene and propane in a Pd membrane reactor. *Chem Eng Sci*. 1996;51:535–547.
19. Sheintuch M. Design of membranal dehydrogenation reactors: the fast reaction asymptote. *Ind Eng Chem Res*. 1998;37:807–814.
20. Casanave D, Ciavarella P, Fiaty K, Dalmon JA. Zeolite membrane reactor for isobutene dehydrogenation: experimental results and theoretical modeling. *Chem Eng Sci*. 1999;54:2807–2815.
21. Illgen U, Schäfer R, Noack M, Kölsch P, Kühnle A, Caro J. Membrane supported catalytic dehydrogenation of iso-butane using an MFI zeolite membrane reactor. *Catal Commun*. 2001;2:339–345.
22. Koumpouras GC, Alpay E, Stepanek F. Mathematical modeling of low-temperature hydrogen production with in situ CO_2 capture. *Chem Eng Sci*. 2007;62:2833–2841.
23. Lattner JR, Harold MP. Comparison of conventional and membrane reactor fuel processors for hydrocarbon-based PEM fuel cell systems. *Int J Hydrogen Energy*. 2004;29:393–417.
24. Brunetti A, Barbieri G, Drioli E, Lee KH, Sea B, Lee DW. WGS reaction in a membrane reactor using a porous stainless steel supported silica membrane. *Chem Eng Process*. 2007;46:119–126.
25. Lee D, Zhang L, Oyama ST, Niu S, Saraf RF. Synthesis, characterization, and gas permeation properties of a hydrogen permeable silica membrane supported on porous alumina. *J Membr Sci*. 2004;231:117–126.
26. Oyama ST, Lee D, Hacarliogly P, Saraf RE. Theory of hydrogen permeability in nonporous silica membranes. *J Membr Sci*. 2004;244:45–53.
27. Schäfer R, Noack M, Kölsch P, Thomas S, Seidel-Morgenstern A, Caro J. Development of a H_2-selective SiO_2-membrane for the catalytic dehydrogenation of propane. *Sep Purif Technol*. 2001;25:3–9.
28. Battersby SE, Miller D, Patch J, Rudolph V, Duke MC, Diniz da Costa JC. Silica membrane reactors for hydrogen processing. *Adv Appl Ceram*. 2007;106:29–34.
29. Sznejer GA, Efremenko I, Sheintuch M. Carbon membranes for high temperature gas separations: experiment and theory. *AIChE J*. 2004;50:596–610.
30. Tiemersma TP, Patil CS, van Sint Annaland M, Kuipers JAM. Modeling of packed bed membrane reactors for autothermal production of ultrapure hydrogen. *Chem Eng Sci*. 2006;61:1602–1616.
31. Ramaswamy RC, Ramachandran PA, Duduković MP. Recuperative coupling of exothermic and endothermic reactions. *Chem Eng Sci*. 2006;61:459–472.
32. Gobina E, Hughes R. Reaction coupling in catalytic membrane reactors. *Chem Eng Sci*. 1996;51:3045–3050.
33. Itoh N, Wu TH. An adiabatic type of palladium reactor for coupling endothermic and exothermic reactions. *J Membr Sci*. 1997;124:213–222.
34. Lin YM, Rei MH. Study on the hydrogen production from methanol steam reforming in supported palladium membrane reactor. *Catal Today*. 2001;67:77–84.
35. Basile A, Tereshenko GF, Orekhova NV, Ermilova MM, Gallucci F, Iulianeli A. An experimental investigation on methanol steam reforming with oxygen addition in a flat Pd-Ag membrane reactor. *Int J Hydrogen Energy*. 2006;31:1615–1622.
36. Chen Y, Xu H, Wang Y, Jin X, Xiong G. Hydrogen production from liquid hydrocarbon fuels for PEMFC application. *Fuel Process Technol*. 2006;87:971–978.
37. Brinkman T, Perera SP, Thomas WJ. An experimental and theoretical investigation of a catalytic membrane reactor for the oxidative dehydrogenation of methanol. *Chem Eng Sci*. 2001;56:2047–2061.
38. Lattner JR, Harold MP. Autothermal reforming of methanol: experiments and modeling. *Catal Today*. 2007;120:78–89.
39. Tomishige K, Nurunnabi M, Maruyama K, Kunimori K. Effect of oxygen addition to steam and dry reforming of methane on bed temperature profile over Pt and Ni catalyst. *Fuel Process Technol*. 2004;85:1103–1120.
40. Frauhammer J, Eigenberger G, Hippel LV, Arntz D. A new reactor concept for endothermic high-temperature reactions. *Chem Eng Sci*. 1999;54:3661–3670.
41. Kolios G, Glöckler B, Gritsch A, Morillo A, Eigenberger G. Heat-integrated reactor concepts for hydrogen production by methane steam reforming. *Fuel Cells*. 2004;5:52–65.
42. Feng W, Tan T, Ji P, Zheng D. Exploration of hydrogen production in a membrane reformer. *AIChE J*. 2006;52:2260–2270.
43. Chen Z, Yan Y, Elnashaie SSEH. Novel circulating fast fluidized-bed membrane reformer for efficient production of hydrogen from steam reforming of methane. *Chem Eng Sci*. 2003;58:4335–4349.
44. Abba IA, Grace JR, Bi HT. Application of the generic fluidized-bed reactor model to the fluidized-bed membrane reactor process for steam methane reforming with oxygen input. *Ind Eng Chem Res*. 2003;42:2736–2745.
45. Patil CS, van Sint Annaland M, Kuipers JAM. Design of a novel autothermal membrane-assisted fluidized-bed reactor for the production of ultrapure hydrogen from methane. *Ind Eng Chem Res*. 2005;44:9502–9512.
46. Avci AK, Trimm DL, İlsen Önsan Z. Heterogeneous reactor modeling for simulation of catalytic oxidation and steam reforming of methane. *Chem Eng Sci*. 2001;56:641–649.
47. Kiatkittipong W, Tagawa T, Goto S, Assabumrungrat S, Silpasup K, Praserthdam P. Comparative study of oxidative coupling of methane: modeling in various types of reactor. *Chem Eng J*. 2005;115:63–71.
48. Hoang DL, Chan SH. Modeling of a catalytic autothermal methane reformer for fuel cell applications. *Appl Catal A Gen*. 2004;268:207–216.
49. Patel KS, Sunol AK. Dynamic behavior of methane heat exchange reformer for residential fuel cell power generation system. *J Power Sources*. 2006;161:503–512.
50. Baldea M, Daoutidis P. Dynamics and control of autothermal reactors for the production of hydrogen. *Chem Eng Sci*. 2007;62:3218–3230.
51. Xu J, Froment GF. Methane steam reforming, methanation and water-gas-shift. I. Intrinsic kinetics. *AIChE J*. 1989;35:88–103.

52. de Smet CRH, de Croon MHJM, Berger RJ, Marin GB, Schouten JC. Design of adiabatic fixed-bed reactors for the partial oxidation of methane to synthesis gas. Application to production of methanol and hydrogen-for-fuel-cells. *Chem Eng Sci*. 2001;56:4849–4861.
53. Trimm DL, Lam CW. The combustion of methane on platinum-alumina fibre catalysts. I. Kinetics and mechanism. *Chem Eng Sci*. 1980;35:1405–1413.
54. Derkx OR, Dixon AG. Effect of the wall Nusselt number on the simulation of catalytic fixed bed reactors. *Catal Today*. 1997;35: 435–442.
55. Dixon AG, Cresswell DL. Theoretical prediction of effective heat transfer parameters in packed beds. *AIChE J*. 1979;25:663–676.
56. Berger RJ, Pérez-Ramírez J, Kapteijn F, Moulijn A. Catalyst performance testing: radial and axial dispersion related to dilution in fixed-bed laboratory reactors. *Appl Catal A Gen*. 2002;227:321–333.
57. Frank-Kamenetski DA. *Diffusion and Heat Exchange in Chemical Kinetics*. Princeton, NY: Princeton University Press, 1955.
58. Kiselev OV. *Theoretical Study of the Phenomena of Heat Waves Movement in Catalyst Bed (in Russian)*. Novosibirsk: Russian Academy of Sciences, Institute of Catalysis, 1993.

Appendix

CO equilibrium conversion derivation

Accounting for both SR and WGS (with the corresponding conversions f_1 and f_2), the overall SR process in equilibrium is described as follows:

$$CH_4 + 2H_2O = CO_2 + 4H_2 \quad (SR)$$

$$CO_2 + H_2 = CO + H_2O \quad (WGS)$$

Then, define the extent of a specie i (ϕ_i) as

$$CH_4\!: \quad \phi_{CH_4} = (1 - f_1) \qquad CO_2\!: \quad \phi_{CO_2} = (f_1 - f_2)$$

$$H_2O\!: \quad \phi_{H_2O} = (2 - 2f_1 + f_2) \quad CO\!: \quad \phi_{CO} = (f_2)$$

To express the H_2 extent, while accounting for H_2 separation, we assume the conditions of the reactor exit in a long reactor, where the H_2 partial pressure in the SR side is equal to that at the membrane side, i.e.,

$$\frac{\phi_{H_2}}{\sum_i \phi_i} = \frac{P_t^M}{P_t^{SR}}, \qquad i = CH_2, H_2O, CO_2, CO, H_2$$

$$\phi_{H_2} = \frac{(3 - 2f_1 + f_2)P_t^M}{(P_t^{SR} - P_t^M)} \tag{A1}$$

The WGS equilibrium constant is

$$K_{WGS} = \frac{p_{CO_2} p_{H_2}}{p_{CO} p_{H_2O}} = 1.26 \times 10^{-2} \exp\left(\frac{4639}{T}\right) \tag{A2}$$

The partial pressure of specie i is expressed as $p_i = \phi_i / \sum_i \phi_i$.

Writing the equilibrium constant in terms of ϕ_i, the following equation, which allows for calculating f_2 for given f_1, P_t^{SR} and P_t^{SR}, is obtained:

$$\frac{(f_1 - f_2)(3 - 2f_1 + f_2)P_t^M}{f_2(2 - 2f_1 + f_2)(P_t^{SR} - P_t^M} = 1.26 \times 10^{-2} \exp\left(\frac{4639}{T}\right) \tag{A3}$$

Then, the equilibrium outlet CO molar flow rate is given by

$$F_{CO} = F_{mf} f_1 f_2 \tag{A4}$$

Front velocity approximation derivation

In the dimensionless form Eqs. 24 and 25 are rewritten as follows:

$$\theta_\tau + \upsilon\theta_\xi - \theta_{\xi\xi} = BW \tag{A5}$$

$$\sigma x_\tau + \beta\upsilon x_\xi = W \tag{A6}$$

The following notation is used:

$$\theta = \frac{\gamma(T - T_f)}{T_f}, \quad \gamma = \frac{E_{Ox}}{R_g T_f}, \quad x = 1 - \frac{y_m^{Ox}}{y_{mf}^{Ox}}, \quad \upsilon = \frac{\overline{v_g}}{\overline{v_{gf}}},$$

$$\xi = \frac{z}{L_0}, \quad \tau = \frac{t}{t_0}, \quad \sigma = \frac{1}{\overline{Le}}, \quad B = \frac{\alpha(-\overline{\Delta H})y_{mf}^{Ox}}{C_{pg}} \frac{\gamma}{T_f},$$

$$W = (1 - x)K, \quad K = \frac{Da}{Pe_T} \exp\left(\frac{\theta}{1 + \theta/\gamma}\right),$$

$$Da = \frac{L}{\overline{v_{gf}}} A_{Ox}^* \exp(-\gamma), \quad Pe_T = \frac{\varepsilon C_{pg} \overline{v_{gf}} L}{(k_{ae}/\rho_g)},$$

The length is scaled by the thermal front width:

$$L_0 = \frac{L}{Pe_T}$$

The time is scaled by the time required to the front to pass the distance equaled to its width ($v_{TF} \approx \overline{v_{gf}}/\overline{Le}$):

$$t_0 = \frac{L_0}{v_{TF}} \approx \frac{\overline{Le}}{Pe_T} \frac{L}{\overline{v_{gf}}}$$

At this point we employ an assumption of an ideal heat front that propagates with a constant velocity v_{TF}. This assumption is valid if the front width is significantly less then the system length, i.e., Pe_T is much higher than 1. The values of Pe_T used in the simulations were in the range of $\approx 10-100$. In a moving frame coordinate system, the ideal front will satisfy the following equations:

$$\theta_{\zeta\zeta} - (\upsilon - \omega)\theta_\zeta = -BW \tag{A7}$$

$$(\beta\upsilon - \sigma\omega)x_\zeta = W \tag{A8}$$

$$\zeta = \xi - \omega\tau, \quad \omega = \frac{v_{TF}\overline{Le}}{\overline{v_{gf}}}$$

$$\zeta \to -\infty\!: \theta_\zeta - \theta \to 0, \; x \to 0; \quad \zeta \to +\infty\!: \theta_\zeta \to 0 \tag{A9}$$

Combining Eqs. A7 and A8 and integrating by ζ from $-\infty$ yields:

$$\theta_\zeta = (\upsilon - \omega)\theta - B(\beta\upsilon - \sigma\omega)x + C \tag{A10}$$

Analysis of boundary conditions at $\zeta \to \infty$ shows that $C = 0$. Applying Eq. A10 at $\zeta \to +\infty$ or at the front position, where $\theta_\zeta = 0$, $\theta = \theta_{\max}$, $x = x_{\max}$, the following relation is obtained:

$$\theta_{\max} = B\frac{(\beta\upsilon - \sigma\omega)}{(\upsilon - \omega)}x_{\max} \tag{A11}$$

Equation A10 can be rewritten by introducing a new variable $u = \theta/\theta_{\max}$ and using Eq. A11, reducing the problem to

$$u_\zeta = \frac{B}{\theta_{\max}}(\beta\upsilon - \sigma\omega)x_{\max}\left(u - \frac{x}{x_{\max}}\right) \tag{A12}$$

$$x_\zeta = \frac{(1-x)K}{(\beta\upsilon - \sigma\omega)} \tag{A13}$$

By dividing Eq. A13 by Eq. A12 the following equation is obtained:

$$\frac{dx}{du} = \frac{(1-x)K\theta_{\max}}{Bx_{\max}(\beta\upsilon - \sigma\omega)^2(u - x/x_{\max})} \tag{A14}$$

Assuming $x_{\max} = 1$, i.e., a complete methane conversion in the Ox reaction (which is supported by the simulations), we obtain:

$$\frac{dx}{du} = p(u)g(u,x), \quad p(u) = \frac{\theta_{\max}K}{B(\beta\upsilon - \sigma\omega)^2}, \quad g(u,x) = \frac{1-x}{u-x} \tag{A15}$$

Note that $g(u, x)$ possesses a singularity if $x \to 1$, while $u \to 1$, however the limits of $g(u, x)$ are finite.

Integrating Eq. A15 from 0 to 1 yields:

$$1 = \int_0^1 p(u)g(u,x)du \tag{A16}$$

For a narrow reaction zone, the main impact into the integral is in the vicinity of the front, where $u \to 1$ and, therefore, $g(u, x) \to 1$. Then, the integral reduces to:

$$1 = \int_0^1 p(u)du = \frac{\theta_{\max}Da}{BPe_T(\beta\upsilon - \sigma\omega)^2}\int_0^1 \exp\left(\frac{\theta_{\max}u}{1 + \theta_{\max}u/\gamma}\right)du \tag{A17}$$

The integral in Eq. A17 is estimated using the narrow reaction zone assumption by expanding the integrant in the vicinity of $u = 1$ (Taylor series, ignoring higher than first-order terms):

$$\begin{aligned}&\int_0^1 \exp\left(\frac{\theta_{\max}u}{1 + \theta_{\max}u/\gamma}\right)du \int_0^1 \exp\left(\frac{\theta_{\max}}{1 + \theta_{\max}/\gamma} + \frac{\theta_{\max}(u-1)}{(1 + \theta_{\max}/\gamma)^2}\right)du \\ &= \exp\left(\frac{\theta_{\max}}{1 + \theta_{\max}/\gamma}\right)\frac{(1 + \theta_{\max}/\gamma)^2}{\theta_{\max}}\left[1 - \exp\left(\frac{-\theta_{\max}}{(1 + \theta_{\max}/\gamma)^2}\right)\right] \sim \exp\left(\frac{\theta_{\max}}{1 + \theta_{\max}/\gamma}\right)\frac{(1 + \theta_{\max}/\gamma)^2}{\theta_{\max}}\end{aligned}$$

Note that the second term in the square brackets is neglected in comparison with 1. Finally, Eq. A17 is reduced to the following algebraic equation:

$$\frac{Da(1 + \theta_{\max}/\gamma)^2}{BPe_T(\beta\upsilon - \sigma\omega)^2}\exp\left(\frac{\theta_{\max}}{1 + \theta_{\max}/\gamma}\right) = 1 \tag{A18}$$

Equations A11 and A18 forms a closed system with respect to two unknown variables ω (front velocity) and $\theta_{\max}$ (maximal temperature).

Manuscript received Nov. 29, 2007, and revision received Apr. 24, 2008.